CORA Cork Open Research Archive
Cartlann Taighde Oscailte Chorcaí

| | |
|---|---|
| Title | A fast electrochemical impedance spectroscopy with a square wave as excitation signal for impedance-based biomedical applications |
| Authors | Wang, Zhongzheng;Shao, Han;O'Riordan, Alan;Higes-Marquez, Javier;O'Connell, Ivan;O'Hare, Daniel |
| Publication date | 2025-06-18 |
| Original Citation | Wang, Z., Shao, H., Riordan, A. O., Higes-Marquez, J., Connell, I. O. and Hare, D. O. (2025) 'A fast electrochemical impedance spectroscopy with a square wave as excitation signal for impedance-based biomedical applications', IEEE Transactions on Biomedical Circuits and Systems, 19(4), pp. 726–742. https://doi.org/10.1109/TBCAS.2025.3579698 |
| Type of publication | Article (peer-reviewed);journal-article |
| Link to publisher's version | 10.1109/tbcas.2025.3579698 |
| Rights | © 2025, IEEE. Personal use of this material is permitted. Permission from IEEE must be obtained for all other uses, in any current or future media, including reprinting/republishing this material for advertising or promotional purposes, creating new collective works, for resale or redistribution to servers or lists, or reuse of any copyrighted component of this work in other works. |
| Download date | 2026-11-02 17:52:22 |
| Item downloaded from | https://hdl.handle.net/10468/17709 |

UCC
University College Cork, Ireland
Coláiste na hOllscoile Corcaigh

This article has been accepted for publication in IEEE Transactions on Biomedical Circuits and Systems. This is the author's version which has not been fully edited and content may change prior to final publication. Citation information: DOI 10.1109/TBCAS.2025.3579698



# A Fast Electrochemical Impedance Spectroscopy with A Square Wave as Excitation Signal for Impedance-based Biomedical Applications

Zhongzheng Wang, *Student Member, IEEE*, Han Shao, *Member, IEEE*, Alan O'Riordan, *Member, IEEE*, Javier Higes-Marquez, *Member, IEEE*, Ivan O'Connell, *Senior Member, IEEE*, and Daniel O'Hare, *Senior Member, IEEE*

***Abstract*—This paper introduces a fast, high-accuracy methodology for conducting Electrochemical Impedance Spectroscopy (EIS) based on Fast Fourier Transform (FFT), to meet the requirements of portable, real-time biomedical impedance-based detections with Ultra-Microband (UMB) sensor. Instead of using white noise-like wideband signals as in conventional FFT-based EIS, the proposed method uses a square wave as the excitation signal, which achieves a fast, accurate EIS measurement, but no longer requires complex circuits like high-resolution DACs or frequency mixers for the signal generation. This work starts with the theoretical justification for treating the sensor as a Linear Time-Invariant (LTI), then the practical linear region for operating the sensor as an LTI system is experimentally verified and determined, which enables the capacity of employing the harmonics of a square wave for EIS measurements. A dynamic model of the charge-transfer resistance together with an approximated of the Constant Phase Element (CPE) are implemented with Verilog-A for simulations, and a circuit consisting of a control amplifier and a Trans-Impedance Amplifier (TIA) is designed and fabricated with 65 nm CMOS for validating its on-chip feasibility. This work shortens the EIS measurement time by 91.7% in a frequency sweep range from 0.5 Hz to 500 Hz, with only 2.73% average Mean Absolute Percentage Error (MAPE), compared to a commercial electrochemical instrument AutoLab, with five pre-modified electrodes across four different concentrations of Ferrocene Carboxylic Acid (FcCOOH), demonstrating this method is suitable for portable, real-time label-free EIS biomedical detections and applications.**

***Index Terms*—Ultra-Microband, CV, EIS, TIA, FFT, Verilog-A, Sensor Modelling**

## I. Introduction

ELECTROCHEMICAL sensors are gaining popularity for a variety of biosensing applications, owing to their high sensitivity, high resolution and fast response [1, 2]. Among various electrochemical detection techniques, Electrochemical Impedance Spectroscopy (EIS) plays a critical role in label-free impedance-based biomedical applications [3]. In label-free sensors, such as those used for DNA detection [4], virus detection [5, 6] or antigen detection [7], particles typically bond to a pre-functionalized electrode, making the electrode surface more insulating and thus increasing the impedance at higher substrate analyte concentrations. In contrast, for an enzymatic or redox-active biosensor (e.g. glucose sensor [8]), the presence of enzymes enhances the redox turnover as the concentration rises, which lowers the electrode-electrolyte impedance at higher concentrations. The fundamentals of EIS can be found in tutorials such as [9–11].

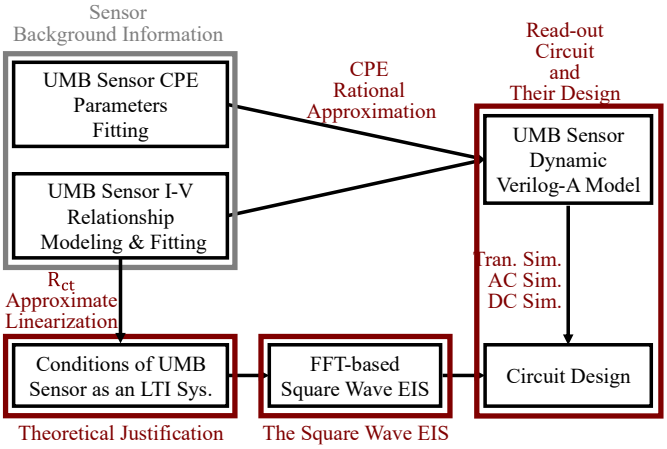



Fig. 1. The overall diagram that indicates the contributions of this work.

Due to advances in CMOS technology, hand-held EIS measurement devices have become realizable and are widely utilized in biomedical applications, including human disease detection and Point-of-Care (PoC) diagnostics [12, 13]. However, their development and popularity are limited by the long measurement time and circuit complexity of conventional EIS methodologies. The EIS employing In-Phase and Quadrature (I/Q Technique) mixing applies a sinusoidal signal to the sensor, and the resulting sensor signal is mixed with in-phase and quadrature reference signals, as discussed in [14–17].

This work is supported by Science Foundation Ireland (SFI) and the Department of Agriculture, Food and the Marine on behalf of the Government of Ireland under the Grand 16/RC/3835 (VistaMilk), and was partly funded by Microelectronic Circuits Centre Ireland (MCCI), through the Enterprise Ireland and IDA Ireland Technology Centers program. *(Corresponding author: Zhongzheng Wang).*

Zhongzheng Wang is with Microelectronic Circuit Center Ireland (MCCI), Tyndall National Institute, Cork, Ireland (e-mail: zhongzheng.wang@mcci.ie).

Han Shao is with Precision Electrochemical Nanosensor Group, Tyndall National Institute, Cork, Ireland (e-mail: han.shao@tyndall.ie).

Alan O'Riordan is with Precision Electrochemical Nanosensor Group, Tyndall National Institute, Cork, Ireland (e-mail: alan.oriordan@tyndall.ie).

Javier Higes-Marquez is with the Precision Electrochemical Nanosensor group, Tyndall National Institute, Cork, Ireland (e-mail: javier.marquez@tyndall.ie).

Ivan O'Connell is with Altera, Cork, Ireland (e-mail: ivan.oconnell@altera.com)

Daniel O' Hare is with Microelectronic Circuit Center Ireland (MCCI), Tyndall National Institute, Cork, Ireland (e-mail: daniel.ohare@mcci.ie).

Authorized licensed use limited to: UNIVERSITY COLLEGE CORK. Downloaded on July 07,2025 at 14:33:53 UTC from IEEE Xplore. Restrictions apply.
© 2025 IEEE. All rights reserved, including rights for text and data mining and training of artificial intelligence and similar technologies. Personal use is permitted, but republication/redistribution requires IEEE permission. See https://www.ieee.org/publications/rights/index.html for more information.

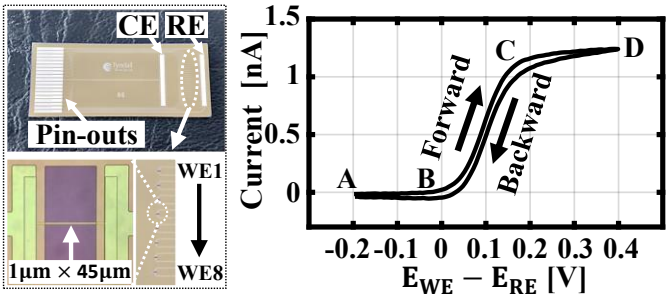
This article has been accepted for publication in IEEE Transactions on Biomedical Circuits and Systems. This is the author's version which has not been fully edited and content may change prior to final publication. Citation information: DOI 10.1109/TBCAS.2025.3579698



While I/Q technique-based EIS excels at detecting electrode impedance in noisy environments —owing to high-performance lock-in amplifiers— it requires mixers, quadrature clock generators and a sinusoidal excitation generator such as a Direct Digital Synthesis (DDS) [18], which adds further complexity to the circuit implementation. Magnitude and Phase Detection (MPD) EIS methodology uses a magnitude detector and a phase detector, each followed by a counter, avoiding the need for quadrature signal generation [19]. Nevertheless, as in I/Q-technique-based systems, the test frequency must be incremented sequentially until the maximum desired frequency is reached, which prolongs the completion of a single EIS measurement and poses disadvantages for real-time EIS applications. Fast Fourier Transform (FFT)-based EIS employs white noise-like wide-band signals such as multi-sine signals [20, 21], chirp-signals [22], system noise [23], pseudo random sequences [24, 25] or other wideband signals [26] as stimuli for EIS measurements, and the impedance is computed by applying an FFT to the input and output sensor signals. This method significantly shortens the measurement time from several hours to a few minutes; however, it relies on a high-resolution, wide-band Digital-to-Analog Converter (DAC) or excitation generator to produce these wide-band signals, thus increasing the circuit complexity. Some bio-impedance techniques discussed in review works [27, 28] inject a square-wave current along with additional analog techniques to mitigate the impact of baseline impedance for a higher dynamic range and SNR [29–31], and to cancel the harmonic error [32] to achieve a higher accuracy or lower power [33, 34], but the proposed methods still need a frequency sweeping, and are not applicable to a label-free EIS detection with a three-electrode system. –Consequently, an EIS methodology with short measurement time, high accuracy, and low complexity is required to enable portable EIS for label-free biomedical applications.

This paper introduces and validates an FFT-based time-domain square-wave EIS methodology that offers advantages in both reducing the measurement time and circuitry complexity. An overall diagram, as is shown in Fig. 1, virtualizes the contributions of this work. In this work, a square wave is used as the sensor excitation signal, and its harmonics are used for computing the EIS via an FFT. To avoid large distortion and the impedance variance due to decreasing AC amplitudes, the conditions where UMB sensor is manipulated as a pseudo LTI system are determined by examining the linear region with both theoretical modeling and experimental tests. Based on the modeling of the charge-transfer resistance of the sensor and the rational approximation of the CPE, a dynamic UMB electrode sensor model is implemented in Verilog-A, offering more realistic UMB sensor behavior and supports multiple simulation analyses for the circuit design, and a circuit consisting of a control amplifier-based potentiostat and a TIA are designed and fabricated in a 65 nm CMOS process, to validate the proposed square-wave EIS approach.

The chip measurement results achieve a high accuracy of 2.73% MAPE, on average, for five pre-deposited UMB




(a). (b).

Fig. 2. (a). A silicon wafer substrate with eight individual UMB electrodes. (b). The measurement results of CV with an UMB electrode sensor in 1 mM FcCOOH dissolved in 10 mM PBS at 25° C, SR = 50 mV/s.

electrodes tested across four FcCOOH concentrations, compared with those from a commercial electrochemical instrument AutoLab. The measurement time is shortened by 91.7% (from 72 seconds to 6 seconds), in a frequency range of 0.5 Hz to 500 Hz. This fast measurement time and high accuracy successfully validate the feasibility of the proposed square-wave EIS for portable, real-time label-free biomedical detection devices.

The remainder of this paper is organized as follows: Section II presents the theory of sensor small-signal linearization and the time-invariant linear region of UMB electrode sensors. Section III introduces the proposed square-wave EIS approach, along with its circuit design and implementation. Section IV describes the experimental results, and Sections V and VI provide the discussion and conclusion, respectively.

## II. Models and the Time-Invariant Linear Region of UMB Electrode Sensors

This section begins by introducing the diffusion mechanisms of UMB electrode sensors, which provide properties essential for theoretical analysis. It then presents the charge-transfer rate model of UMB electrode sensors and its small-signal linearization. Finally, the practical linear region and the biasing conditions where square-wave EIS can be applied are experimentally verified.

### *A. UMB Sensors and their Diffusion Mechanisms*

The UMB electrochemical sensors were fabricated on a silicon wafer substrate with eight individual gold UMB Working Electrodes (WEs) (1 μm × 45 μm × 150 nm), a shared platinum pseudo Reference Electrode (RE) (500 μm × 10 mm × 150 nm) and a shared platinum Counter Electrode (CE) (500 μm × 10 mm × 150 nm), as is shown in Fig. 2(a). 19-pin Mini HDMI-compatible pin-outs were integrated at the edge of the chip, allowing for external electrical connections.

A typical Cyclic Voltammetry (CV) measurement of an UMB electrode sensor is shown in Fig. 2(b). Unlike other electrodes, which typically exhibit a “duck-shaped” current response, UMB electrode sensors show a “sigmoidal” profile, due to their uniform three-dimensional radial diffusion mechanism near the electrode-electrolyte interface. In this radial diffusion mechanism, the diffusion layer thickness near the UMB electrode is thin, stable and exceeds the electrode physical size, which guarantees the mass can effectively

Authorized licensed use limited to: UNIVERSITY COLLEGE CORK. Downloaded on July 07,2025 at 14:33:53 UTC from IEEE Xplore. Restrictions apply.
© 2025 IEEE. All rights reserved, including rights for text and data mining and training of artificial intelligence and similar technologies. Personal use is permitted, but republication/redistribution requires IEEE permission. See https://www.ieee.org/publications/rights/index.html for more information.

This article has been accepted for publication in IEEE Transactions on Biomedical Circuits and Systems. This is the author's version which has not been fully edited and content may change prior to final publication. Citation information: DOI 10.1109/TBCAS.2025.3579698



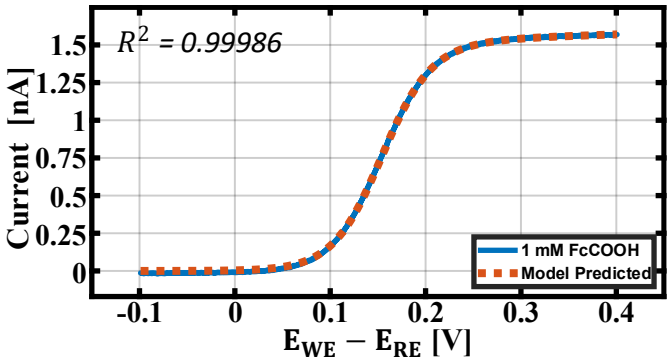



Fig. 3. The measurement results of CV for one cycle with an UMB electrode sensor in 1 mM FcCOOH dissolved in 10 mM PBS at 25° C, SR = 0.001 V/s, and the model predicted data.

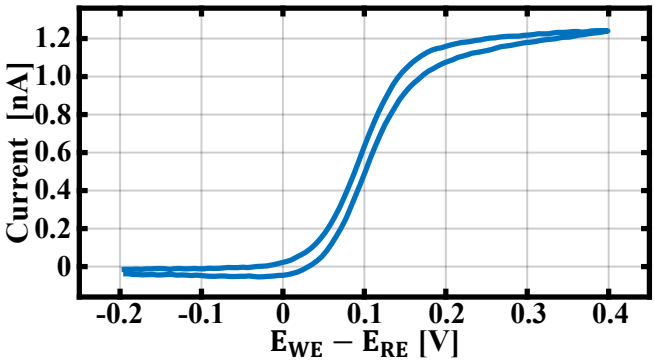



Fig. 4. The CV measurement result under experimental conditions of 1 mM FcCOOH dissolved in 10 mM PBS at 25° C, with a SR of 50 mV/s.

transfer from the bulk to the electrode surface, as demonstrated in [35]. Consequently, the rate of the species replenishment is sufficiently rapid and stable to maintain an adequate analyte concentration at the electrode-electrolyte surface of the UMB electrodes, yielding a steady-state current as indicated from C to D in Fig. 2(b), where the current level doesn't drop with higher electrode potential after the peak current during a CV measurement, unlike other macro electrodes such as [36, 37].

Due to the unique three-dimensional radial diffusion mechanism, the sensor current of an UMB electrode is no longer limited by the mass diffusion effect [38], which enables straightforward high-speed kinetic studies, and achieves enhanced current density, higher Signal-to-Noise Ratio (SNR), shorter analysis time and low-volume analysis for on-chip sensor integration [39].

*B. Charge-transfer Rate Model of UMB Electrode Sensors and its Small-signal Linear Approximation*

The charge-transfer rate at the electrode-electrolyte interface, at which the electrochemical reaction takes place, can be represented by the reciprocal current relation as described in (1) [40]:

$$I_{tot}(E) = \left(\frac{1}{I_{mt}(E)} + \frac{1}{I_{et}(E)}\right)^{-1}, \quad (1)$$

where $I_{mt}(E)$ is the mass-transportation-controlled current, $I_{et}(E)$ is the electron-transfer-controlled current, and $E$ is the applied electrode potential.

In a static liquid, reactants are consumed at the electrode surface, producing a concentration difference between the electrode surface and the bulk solution. The established concentration gradient drives reactants toward the electrode surface while causing products to diffuse away into the bulk. In the case of a high-rate charge transfer at the electrode surface, the mass diffusion arising from this concentration gradient becomes the primary mechanism that limits the maximum current. Considering the scenario in which only the Reduced Species (Red) are initially present, and the Oxidized Species (Ox) are absent but produced at the electrode surface via electrochemical reactions, the net mass-transportation-limiting current, $I_{mt}$, is given by (2):

$$I_{mt} = nFAm_R[C_R^* - C_R(x=0)], \quad (2)$$

and (3):

$$I_{mt} = nFAm_O C_O(x=0). \quad (3)$$

For $C_R(x=0) \ll C_R^*$, the maximum possible net oxidation current, also defined as the limiting current, $I_l$, is given by:

$$I_l = nFAm_R[C_R^* - C_R(x=0)] \approx nFAm_R C_R^*, \quad (4)$$

where $A$ is the active electrode area, $F$ is the Faraday constant, $n$ is the number of electrons transferred in the reaction, $m_R$ and $m_O$ are the mass-transfer coefficients of Red and Ox respectively, $C_R^*$ and $C_O^*$ are the bulk concentrations of Red and Ox respectively, and $C_R(x=0)$ and $C_O(x=0)$ are the Red and Ox concentrations at the electrode surface respectively.

Due to the high-efficiency mass transportation mechanism of UMB electrode sensors, the system can be approximated to a reversible, or a quasi-reversible system [38]. Consequently, by substituting (2), (3) and (4) into the Nernst Equation [41], the mass-transportation-controlled current can be approximated by (5), with a practical condition of $m_R \approx m_O$.

$$I_{mt}(E) = \frac{I_l}{1 + \frac{m_R}{m_O} e^{-\frac{nF(E-E_0)}{RT}}} \approx \frac{I_l}{1 + e^{-\frac{nF(E-E_{1/2})}{RT}}} \quad (5)$$

where $E_0$ is the formal potential, which is approximately equal to the half potential, $E_{1/2}$ [42], the applied potential where $I_{mt} = I_l/2$.

The charge-transfer kinetics at the electrode-electrolyte interface can be described with Butler-Volmer equations [43]:

$$I_{et}(E) = nFAk_0\left[e^{\frac{\alpha nF}{RT}(E-E_0)} - e^{\frac{(1-\alpha)nF}{RT}(E-E_0)}\right], \quad (6)$$

where $k_0$ is the standard rate constant of the electrode reaction, and $\alpha$ is the transfer coefficient, $0 < \alpha < 1$.

For voltammetry measurements conducted at slow Scan Rates (SR) ($\leq 50\ mV$ per second), each small applied potential step allows the system to nearly re-equilibrate owing to the high-efficient mass transportation, which ensures that the analyte concentration at the electrode surface closely tracks the bulk concentration. Consequently, the large-signal non-linear kinetic behavior of the UMB electrode sensors can be

Authorized licensed use limited to: UNIVERSITY COLLEGE CORK. Downloaded on July 07,2025 at 14:33:53 UTC from IEEE Xplore. Restrictions apply.
© 2025 IEEE. All rights reserved, including rights for text and data mining and training of artificial intelligence and similar technologies. Personal use is permitted, but republication/redistribution requires IEEE permission. See https://www.ieee.org/publications/rights/index.html for more information.

This article has been accepted for publication in IEEE Transactions on Biomedical Circuits and Systems. This is the author's version which has not been fully edited and content may change prior to final publication. Citation information: DOI 10.1109/TBCAS.2025.3579698



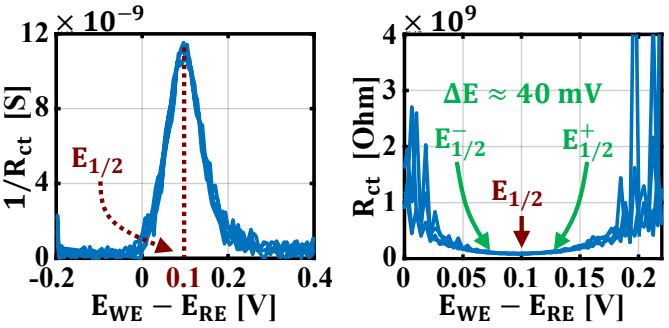



Fig. 5. The determination of the conditions where $R_{ct}$ is an LTI component. (a). The conductance of the UMB electrode sensor is potential-dependent. (b). Determination of the practical time-invariant linear region.

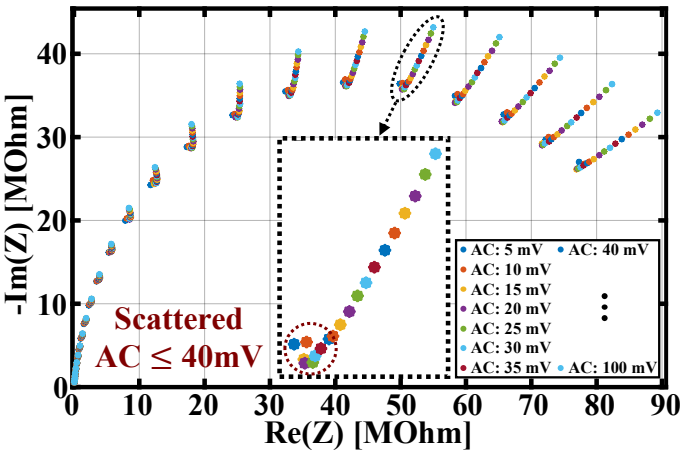



Fig. 6. EIS results of UMB electrode with AC amplitude increasing from 5 mV to 100 mV, with an incremental step of 5 mV at 0.1 V DC potential.

mathematically modeled via Butler-Volmer relationships and Nernst Equation considering equations (1), (5) and the oxidation counterpart of (6), as is described in (7) [44]:

$$I_{tot}(E) = \frac{I_{mt}}{1 + e^{-\frac{nF}{RT}(E-E_0)} + K_0 e^{-\frac{nF}{RT}(1-\alpha)(E-E_0)}}, \quad (7)$$

where $K_0 = I_{mt}/nFAC_R^* k_0$ is the dimensionless rate constant, whose smaller value indicates the system is more reversible.

This charge-transfer rate model of the UMB electrode sensor is validated using CV under the experimental conditions of 1 mM FcCOOH dissolved in 10 mM Phosphate Buffered Saline (PBS) at 25 °C, employing an extremely slow scan rate of 0.001 V/s to minimize double-layer charging currents. The model is fitted by applying the Levenberg–Marquardt algorithm, using an approximate active electrode area $A$ of $5.85 \times 10^{-11}$ m$^2$. The fitted parameters $I_{mt}$, $E_0$, $\alpha$ and $k_0$ are 1.62 nA, 0.155 V, 0.90, and 0.3 cm/s, respectively, and yield an overall correlation coefficient of $R^2$ = 0.99986, demonstrating excellent agreement between the model and the experimental data, as is shown in Fig. 3.

To obtain the large-signal non-linear charge-transfer resistance model, $R'_{ct}(E)$, one first takes the derivative of (7) with respect to $E$, and then forms its reciprocal, as described in (8).

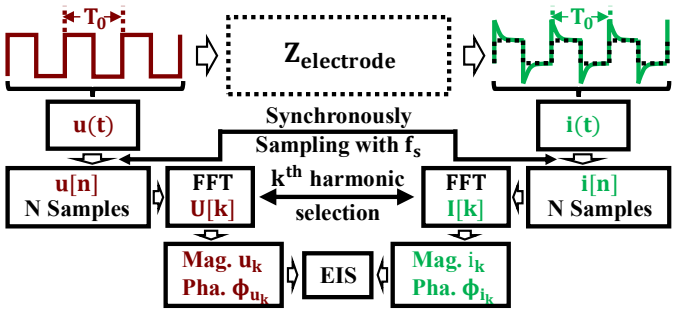



Fig. 7. The system level diagram of the proposed square-wave EIS.

$$R'_{ct}(E) = 1/\frac{dI_{tot}(E)}{dE} = \frac{\left\{1 + e^{-\frac{nF(E-E_0)}{RT}} + K_0\left[e^{-\frac{nF(E-E_0)}{RT}}\right]^{1-\alpha}\right\}^2}{I_{mt}\left[\frac{nF}{RT}e^{-\frac{nF(E-E_0)}{RT}} + \frac{nF}{RT}K_0(1-\alpha)\left(e^{-\frac{nF(E-E_0)}{RT}}\right)^{1-\alpha}\right]} \quad (8)$$

For a reversible or quasi-reversible system, the standard rate constant $K_0 \ll 1$, and the equation is simplified to (9):

$$R'_{ct}(E) \approx \frac{2RT\left[1 + \cosh\frac{nF(E-E_0)}{RT}\right]}{nF \cdot I_{mt}}, \quad (9)$$

where the model shows non-linearities.

It can be seen that $R'_{ct}$ reaches minimum around $E_0$, or $E_{1/2}$, indicating a maximum AC voltage-to-current gain (sensor transconductance) for a higher SNR at the sensor output current for the same small level of applied electrode potential perturbation. In addition, due to the symmetry of the hyperbolic cosine function, the maximum allowable potential swing over which $R'_{ct}$ remains relatively constant is larger than at other selected potentials in the model. Therefore, $E_{1/2}$ has advantages in different aspects to be chosen as the DC bias in small-signal linearization.

To linearize the $R'_{ct}$ to its corresponding small-signal linear charge-transfer resistance model, $R_{ct}$, a First Order Taylor Approximation is applied to (8) at $E_{1/2}$, as is shown in (10).

$$R_{ct}(E_{1/2}) \approx \frac{\Delta E}{I_{tot}(E_{1/2} + \Delta E/2) - I_{tot}(E_{1/2} - \Delta E/2)} = \frac{RT(2+K_0)^2}{nF \cdot I_{mt}(1 + K_0 - \alpha K_0)} \approx \frac{RT4}{nF \cdot I_{mt}}|_{K_0 \ll 1} \quad (10)$$

It can be seen that the $R_{ct}$ around $E_{1/2}$ is linearly approximated as an electrode potential-independent value, enabling the use of a wideband signal containing harmonic frequencies of varying amplitude.

### *C. Practical Time-Invariant Linear Region of UMB Electrode Sensors for EIS*

In a practical EIS measurement, the maximum allowable AC magnitude for EIS is constrained by the region in which $R_{ct}$

Authorized licensed use limited to: UNIVERSITY COLLEGE CORK. Downloaded on July 07,2025 at 14:33:53 UTC from IEEE Xplore. Restrictions apply.
© 2025 IEEE. All rights reserved, including rights for text and data mining and training of artificial intelligence and similar technologies. Personal use is permitted, but republication/redistribution requires IEEE permission. See https://www.ieee.org/publications/rights/index.html for more information.

This article has been accepted for publication in IEEE Transactions on Biomedical Circuits and Systems. This is the author's version which has not been fully edited and content may change prior to final publication. Citation information: DOI 10.1109/TBCAS.2025.3579698



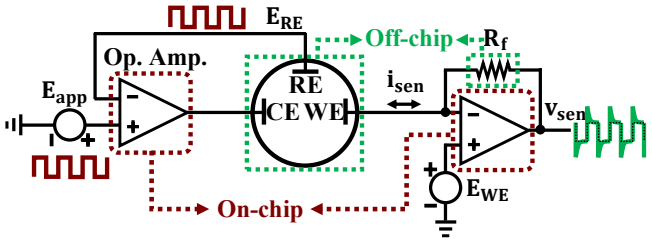



Fig. 8. The block diagram of the circuit for the proposed square-wave EIS.

remains independent of the electrode potential. In a CV measurement result under experimental conditions of 1 mM FcCOOH dissolved in 10 mM PBS at 25 °C, with a SR of 50 mV/s, shown in Fig. 4, the DC operating point, $E_{1/2}$, is chosen to be 0.1 V where the transconductance reaches maximum, as is shown in Fig. 5(a). The maximum allowable AC potential amplitude, $\Delta E \approx E_{1/2}^{+} - E_{1/2}^{-}$, is determined to be 40 mV, where the vicinity of $E_{1/2}$ at which the $R_{ct}$ remains relatively constant, as is shown in Fig. 5(b).

The linear region is verified through EIS measurements on an AutoLab instrument at a DC potential of 0.1 V, while incrementing the AC amplitude from 5 mV to 100 mV in 5 mV steps. Fig. 6 presents the resulting EIS data.

It can be observed that for AC amplitudes below 40 mV, the impedance exhibits a scattered distribution; however, as the AC amplitude increases beyond this threshold, a significant increase in impedance is noted, signaling a transition of $R_{ct}$ into the non-linear region. To quantitatively characterize the sensor's impedance variations, the MAPE is computed using the impedance at an AC amplitude of 5 mV as a reference, as shown in Table I. The MAPE increases considerably (over 5% [24, 25, 45]) when the AC amplitude is beyond 40 mV, indicating the upper limit of the acceptable AC amplitude. In addition, it can be seen that the double-layer near the electrode surface is relatively constant due to the negligible emergence of a phase shift. Consequently, within this identified region, the UMB electrode sensor can be treated as an LTI system, which underpins the use of a square-wave excitation —whose harmonic magnitudes diminish at higher harmonic frequencies— to perform EIS.

TABLE I. MAPE OF THE IMPEDANCE WITH SCANNING AC AMPLITUDE

| AC Amplitude | MAPE | AC Amplitude | MAPE |
|---|---|---|---|
| **10 mV** | **1.29 %** | 60 mV | 6.70 % |
| **15 mV** | **2.45 %** | 65 mV | 7.31 % |
| **20 mV** | **2.69 %** | 70 mV | 7.73 % |
| **25 mV** | **3.28 %** | 75 mV | 8.26 % |
| **30 mV** | **3.58 %** | 80 mV | 8.85 % |
| **35 mV** | **3.99 %** | 85 mV | 9.50 % |
| **40 mV** | **4.57 %** | 90 mV | 10.21 % |
| 45 mV | 5.14 % | 95 mV | 10.86 % |
| 50 mV | 5.65 % | 100 mV | 11.40 % |
| 55 mV | 6.12 % | | |

## III. THE PROPOSED SQUARE WAVE EIS AND ITS CIRCUIT IMPLEMENTATION

### *A. Proposed Square-wave EIS via an FFT*

The proposed EIS employs a square-wave excitation, and the

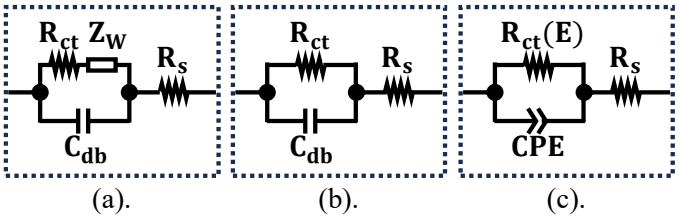



Fig.9. Models of electrochemical sensor electrode-electrolyte interfaces: (a). Randle's Model. (b). Randle's Model with Warburg Impedance omitted. (c). Model with CPE, where $R_{ct}$ is dynamic.

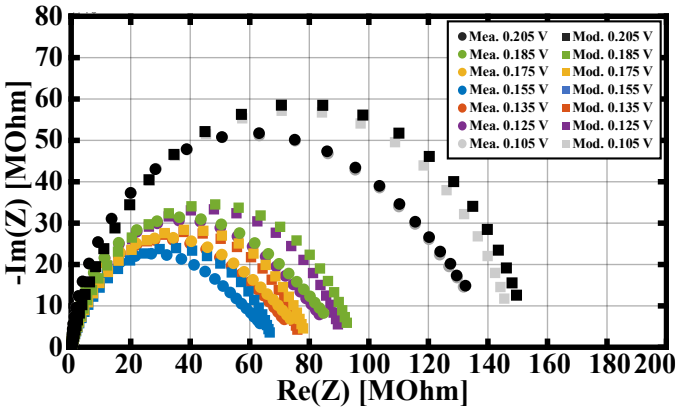



Fig. 10. EIS measurement results with an amplitude of 10 mV over a frequency range of 0.1 Hz to 100 kHz, vs. Verilog-A model-predicted results from Cadence, on the DC biases of 0.105 V, 0.125 V, 0.135 V, 0.155 V, 0.175 V, 0.185 V and 0.205 V over the same frequency range.

impedance at the electrode-electrolyte interface is calculated by dividing the complex value of the selected harmonic tones obtained after applying an FFT to both the input and output signals. Fig. 7 shows the block diagram of the proposed approach, and Fig. 8 shows the circuit blocks, where a control amplifier acts as the potentiostat and a resistive TIA converts the sensor current into voltage, which will then be sampled by a data acquisition circuitry like an ADC.

The DC operating point where the sensor is linearized is determined to be the potential where $R_{ct}$ reaches minimum, and the maximum AC potential amplitude is determined by identifying the vicinity of the DC operating point at which $R_{ct}$ remains relatively constant, as discussed in Section II.

The input and output are synchronously sampled with a sampling rate of $f_s$ for N samples, and the FFT, expressed in complex format in (11) through Euler's equation, is employed to compute the EIS:

$$X[k] = \sum_{n=0}^{N-1} s[n] \cos\left(2\pi \frac{kn}{N}\right) - j \sum_{n=0}^{N-1} s[n] \sin\left(2\pi \frac{kn}{N}\right) \quad (11)$$

where $U[k]$ and $I[k]$ represent the $k^{th}$ point in the FFT of the sampled input signal, $u[n]$, and the sampled response signal, $i[n]$, respectively. Since the FFT of a square wave has components only at odd harmonics of the fundamental frequency, $f_0$, namely, $(2m-1)2\pi f_0$, where $m$ is an integer number, the tones selected for computing the EIS are given by:

$$k = \frac{(2m-1) \cdot f_0}{f_s} \cdot N, \quad (12)$$

Authorized licensed use limited to: UNIVERSITY COLLEGE CORK. Downloaded on July 07,2025 at 14:33:53 UTC from IEEE Xplore. Restrictions apply.
© 2025 IEEE. All rights reserved, including rights for text and data mining and training of artificial intelligence and similar technologies. Personal use is permitted, but republication/redistribution requires IEEE permission. See https://www.ieee.org/publications/rights/index.html for more information.

This article has been accepted for publication in IEEE Transactions on Biomedical Circuits and Systems. This is the author's version which has not been fully edited and content may change prior to final publication. Citation information: DOI 10.1109/TBCAS.2025.3579698



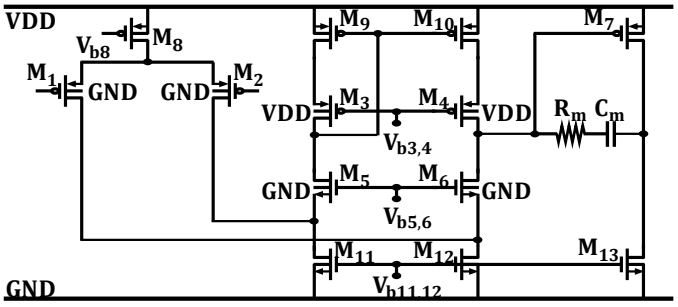



Fig. 11. PMOS-input folded-cascode amplifier topology, complemented by a CS output stage with Miller compensation.

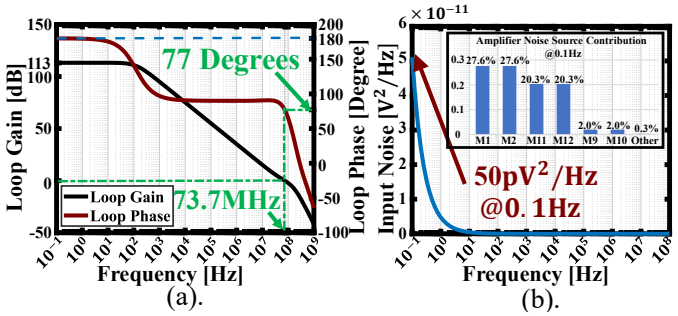



Fig. 12. (a). Stability analysis, and (b). input-referred voltage noise density spectrum and the noise source contribution of the in-band integrated noise.

and the EIS of the electrode-electrolyte interface at each harmonic frequency of the square wave is determined by (13). The frequency range of square wave EIS is from $f_0$ to $f_s/2$:

$$Z_{(2m-1)^{th}} = \frac{U[k]}{I[k]} \tag{13}$$

Due to the fact that a square wave can be easily generated by a simple single-bit DAC, such as switches, the complexity of EIS circuitry can be considerably reduced, and the measurement time is significantly shortened, due to the quick computation of applying an FFT.

*B. Verilog-A Model of UMB Sensor for Circuit Design*

As described in Section II, the charge-transfer resistance of an UMB sensor can be expressed in (10); therefore, providing a possibility to implement the sensor with Verilog-A in simulator for a more accurate circuit design.

Unlike the conventional sensor models in Fig. 9(a) and (b) [46], the model employed in this work comprises a dynamic charge-transfer resistance and a CPE, as shown in Fig. 9(c).

This approach accommodates real world sensors and their associated variability, yielding greater robustness in the circuit design. The Warburg Impedance, $Z_W$, is omitted owing to the highly efficient mass transportation [47].

CPE is a phenomenological mathematical equation, modeled by (14) [48], where $Q$ and $\gamma$ are the CPE parameters, and $s = j\omega$. It reflects an overall macroscopic response of the electrode surface's non-uniformity, roughness, and even porosity. It cannot be described by a finite number of discrete resistors or capacitors with frequency-independent values, due to the fact that each local sub-microscopic region effectively introduces its own RC combination.

$$CPE = \frac{1}{Q \cdot s^{\gamma}} \tag{14}$$

Since the fractional order factor, $s^{\gamma}$, cannot be directly simulated by Computer-Aided Design (CAD) tools such as Cadence, and its physical mechanism is still not clear [48, 49], the CPE must be approximated to a rational polynomial expression.

RC combinations have been proposed in [50–52] to model the CPE, but their inaccuracy limits their usability in most applications and circuit analysis. Another study [53] achieved a precise fitting of the CPE using adaptive Antoulas–Anderson (AAA) algorithm with an approximate rational function over a broader frequency range; but a potential of none-convergence may exist like other fitting algorithms [54, 55] for a higher order of a rational function. To obtain an accurate approximation of the CPE in a sufficient bandwidth of 0.1 Hz to 1 GHz for the square-wave EIS circuitry design, for simplicity, Modified Oustaloup Recursive Approximation (MORA) is utilized, as expressed in (15) [56]. MORA is a numerical computation that avoids the potential non-convergence like a fitting algorithm, while still delivering a suitably accurate approximation.

TABLE II. THE ABSOLUTE PERCENTAGE ERROR

| DC (V) | $R_{ct,mea}$ (MΩ) | $R_{ct,mod}$ (MΩ) | APE % |
|---|---|---|---|
| **0.105** | 131.83 | 145.7 | 10.21 |
| **0.125** | 83.36 | 89.72 | 7.34 |
| **0.135** | 71.62 | 76.07 | 5.91 |
| **0.155** | 63.44 | 66.77 | 4.96 |
| **0.175** | 73.61 | 77.99 | 5.67 |
| **0.185** | 84.79 | 92.71 | 9.05 |
| **0.205** | 132.45 | 149.80 | 12.79 |

$$s^{\gamma} \approx \left(9 \cdot \frac{\omega_h}{10}\right)^{\gamma} \left(\frac{9s^2 + 10\omega_h s}{9(1-\gamma)s^2 + 10\omega_h s + 9\gamma}\right) \prod_{k=1}^{N} \frac{s + \omega_k'}{s + \omega_k} \tag{15}$$

where $\gamma \in (0,1)$ to ensure the filter is stable, $\omega_h$ and $\omega_b$ are the upper bound and lower bound of the target angular frequency range respectively, and $\omega_k'$ and $\omega_k$ are the poles and zeros of the transfer function respectively:

$$\omega_k' = \omega_b \omega_u^{(2k-1-\gamma)/N}, \tag{16}$$

$$\omega_k = \omega_b \omega_u^{(2k-1+\gamma)/N}, \tag{17}$$

with $\omega_u = \sqrt{\omega_h/\omega_b}$, and the approximated CPE is expressed by (18):

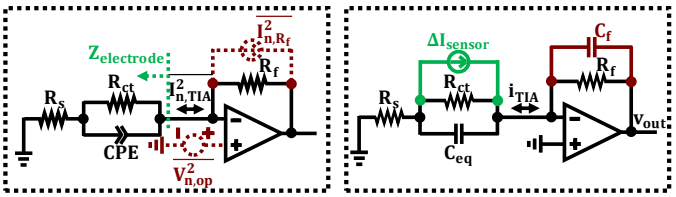
$$\begin{aligned} CPE &\approx Q^{-1}(s^{\gamma})^{-1} \\ &\approx Q^{-1}\left(\frac{9\omega_h}{10}\right)^{-\gamma} \left(\frac{9(1-\gamma)s^2 + 10\omega_h s + 9\gamma}{9s^2 + 10\omega_h s}\right) \prod_{k=1}^{N} \frac{s + \omega_k}{s + \omega_k'}. \end{aligned} \tag{18}$$

Together with an implementation of equation (7) via a non-linear voltage-dependent current source, and a Laplace Impedance Filter for the approximated CPE, the model shown in Fig. 9(c) thus can be realized in Verilog-A for running simulations that reflect practical sensor behavior. A validation

Authorized licensed use limited to: UNIVERSITY COLLEGE CORK. Downloaded on July 07,2025 at 14:33:53 UTC from IEEE Xplore. Restrictions apply.
© 2025 IEEE. All rights reserved, including rights for text and data mining and training of artificial intelligence and similar technologies. Personal use is permitted, but republication/redistribution requires IEEE permission. See https://www.ieee.org/publications/rights/index.html for more information.

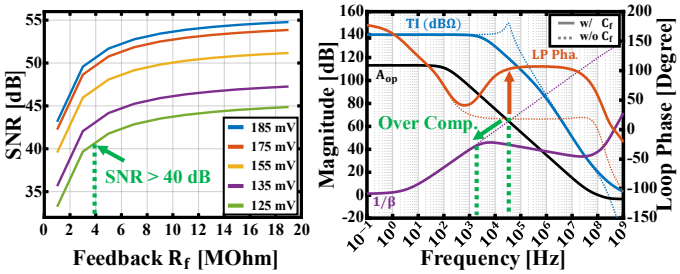
This article has been accepted for publication in IEEE Transactions on Biomedical Circuits and Systems. This is the author's version which has not been fully edited and content may change prior to final publication. Citation information: DOI 10.1109/TBCAS.2025.3579698






(a). (b).

Fig. 13. The equivalent models for TIA design. (a). The simplified equivalent model with noise source contributions, and (b). the equivalent model for analyzing stability and bandwidth.




(a). (b).

Fig. 14. (a). The SNR analysis of TIA at a DC bias of 0.125 V, 0.135 V, 0.155 V, 0.175 V and 0.185 V. (b). The stability analysis of TIA with overcompensation.

of the proposed Verilog-A model is shown in Fig. 10, whose DC operating points for running EIS are chosen to be 0.105 V, 0.125 V, 0.135 V, 0.155 V, 0.175 V, 0.185 V and 0.205 V from Fig. 3, and the CPE parameters are obtained through optimized fittings with a commercial AutoLab instrument based on sensor-measured EIS data. The absolute percentage errors (APE) between the measured charge-transfer resistance, $R_{ct,mea}$, and the simulated charge-transfer resistance from the Verilog-A model, $R_{ct,mod}$, at 0.1 Hz, evaluated under various DC biases, are summarized in Table II.

TABLE III. THE OPERATION REGIONS OF TRANSISTORS

| Transistors | Region | $g_m/I_d$ |
|---|---|---|
| $M_1, M_2, M_7$ | Moderate inversion region | 16 |
| $M_3 \sim M_6$ | Moderate inversion region | 18 |
| $M_8 \sim M_{13}$ | Strong inversion region | 10 |

It can be observed that the proposed dynamic Verilog-A model of the UMB electrode sensor exhibits stronger agreement with the measured sensor data in the linear region (1.55 mV ± 20 mV). In addition, compared to a model with a capacitor, the CPE more accurately reflects the double-layer behavior near the electrode-electrolyte interface [48, 53], which improves the accuracy of the circuit design.

### *C. Design of the Amplifier*

The potentiostat and the TIA employ the same amplifier topology. To minimize the impact of flicker noise within the target bandwidth ranging from sub-Hz to 1 kHz, the amplifier is designed with a PMOS-input folded-cascode topology, complemented by a Common Source (CS) output stage to enlarge the DC gain and output swing, as is shown in Fig. 11.

The transistors designated for amplification ($M_1, M_2, M_7$) and for cascode stage ($M_3 \sim M_6$) are biased in the moderate-inversion region for a larger $g_m/I_d$ to ensure noise, power and speed optimization, while the transistors ($M_8 \sim M_{13}$) serving as current sources are set to be in strong-inversion region for minimizing the current noise, with long transistor channel lengths to reduce the effects of random mismatches. Table III summarizes the regions of operation for the MOSFET devices within the amplifier. The Gain Bandwidth (GBW), attenuated due to the large aspect ratio of those transistors in moderate inversion, can be compensated with a larger $g_m$ of input pairs of both two stages through a high DC biasing current. The Miller compensation is utilized to do the pole splitting and right-hand-side zero cancellation, ensuring its stability. Comprehensively, the amplifier achieves a GBW of 73.7 MHz with 77° of phase margin with a capacitive load of 2 pF, and a DC gain of 113 dB, as is shown in Fig. 12(a). The dominant noise sources are the flicker noise contributions from the differential input pair and current sources, resulting in a total in-band input-referred voltage noise power of $4.12 \times 10^{-11}$ V$^2$, where the input-referred voltage noise density spectrum and the noise source contribution of the in-band integrated noise are shown in Fig. 12(b). The total power is 1.25 mW.

### *D. Design of the TIA*

The design of the TIA entails the decision of the feedback capacitor, $C_f$, and feedback resistor, $R_f$, with an emphasis on noise, bandwidth and stability considerations.

The minimum value of $R_f$ is determined by the noise requirements, and the corresponding simplified equivalent model for noise analysis of a TIA-based electrochemical system is shown in Fig. 13(a). Taking into account noise contributions from the amplifier and the feedback resistor, the input-referred current noise power density of the TIA, $\overline{I_{n,TIA}^2}$, is expressed by (19):

$$\begin{aligned}\overline{I_{n,TIA}^2} &= \overline{V_{n,op}^2} \cdot \left|1 + \frac{R_f}{Z_{electrode}}\right|^2 \cdot \frac{1}{R_f^2} + \frac{4KT}{R_f} \\ &= \overline{V_{n,op}^2}\left[\frac{1}{R_{ct}^2} + \frac{1}{R_f^2} + \frac{2}{R_{ct}R_f} + Q^2\omega^{2\gamma} \right. \\ &\quad \left. + \omega^{\gamma} 2Q \cos\frac{\alpha\pi}{2}\left(\frac{1}{R_{ct}} + \frac{1}{R_f}\right)\right] + \frac{4KT}{R_f}, \end{aligned} \quad (19)$$

where $\overline{V_{n,op}^2}$ represents the input-referred voltage noise power density of the amplifier, K is the Boltzmann constant, T is the temperature in Kelvin, and $Z_{electrode}$ represents the AC small-signal impedance looking into the working electrode, which is expressed by $R_{ct}/[1 + QR_{ct}(j\omega)^{\gamma}]$.

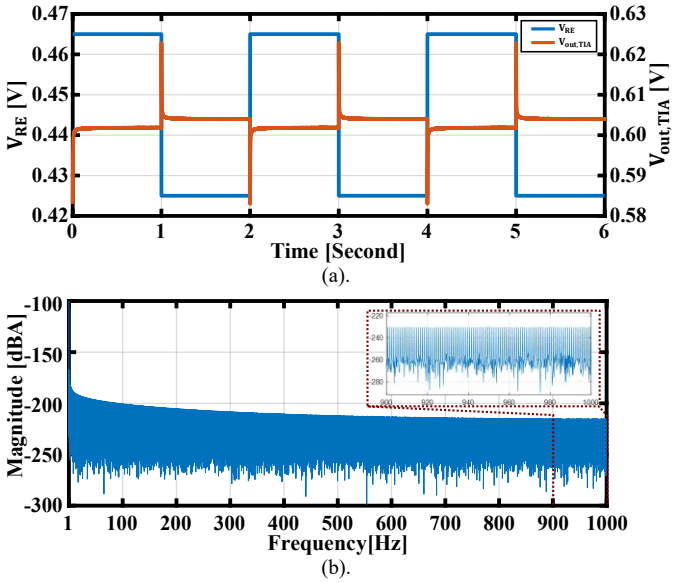
The feedback resistor, $R_f$, is determined by analyzing two noise-related aspects: (i). the SNR between the sensor's DC bias current, $I_{sensor}$, and the circuit's in-band integrated noise as expressed in (20), and (ii). the SNR of the highest-frequency harmonic in the TIA output relative to the noise floor, determined via an FFT.

The parameters $I_{sensor}$, $R_{ct}$, and CPE are obtained by selecting different DC operating points in the Verilog-A model fitted to the data in Fig. 3. For noise integration, the bandwidth is chosen to be 0.1 Hz to 1 kHz, which is twice the range of 0.1 Hz to 500 Hz for the target UMB sensor in this work

Authorized licensed use limited to: UNIVERSITY COLLEGE CORK. Downloaded on July 07,2025 at 14:33:53 UTC from IEEE Xplore. Restrictions apply.
© 2025 IEEE. All rights reserved, including rights for text and data mining and training of artificial intelligence and similar technologies. Personal use is permitted, but republication/redistribution requires IEEE permission. See https://www.ieee.org/publications/rights/index.html for more information.

This article has been accepted for publication in IEEE Transactions on Biomedical Circuits and Systems. This is the author's version which has not been fully edited and content may change prior to final publication. Citation information: DOI 10.1109/TBCAS.2025.3579698






(a).

(b).

Fig. 15. The noise analysis considering the FFT demodulation; (a). the simulated time-domain response of the Verilog-A model, with a DC potential ($V_{WE} - V_{RE}$) of 155 mV, and an AC amplitude of 40 mV–, and (b). the FFT results of the current, by converting the TIA output with an $R_f$ of 4 MOhm.

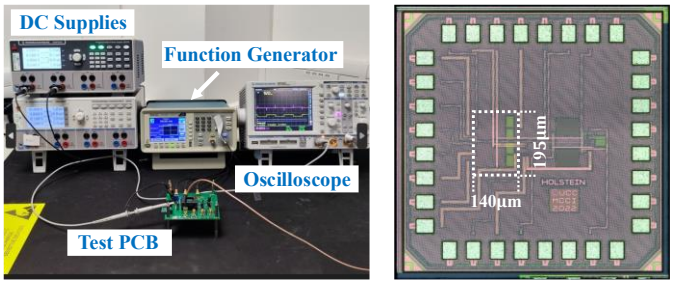
$$SNR = 10\log_{10}\left[\frac{I_{sensor}^2}{\int_{\omega_b}^{\omega_h}\overline{I_{n,TIA}^2}}\right] \geq 40, \qquad (20)$$

where $\int_{\omega_b}^{\omega_h}\overline{I_{n,TIA}^2}$ is the in-band integrated noise power of the TIA, and $\omega_b$ and $\omega_h$ represent the angular frequencies corresponding to the lower and higher bounds of the target bandwidth, respectively.

The SNR was simulated by sweeping $R_f$ from 1 MOhm to 20 MOhm at five DC sensor biases (0.125 V, 0.135 V, 0.155 V, 0.175 V and 0.185 V), covering the sensor linear region as discussed in Section II. The in-band integrated noise is designed to be 40 dB lower than the sensor DC current power, $I_{sensor}^2$, to enable robust performance. The simulated SNR results, shown in Fig. 14(a), indicate that a $R_f$ value of at least 4 MOhm is required to achieve an SNR exceeding 40 dB.

To evaluate the SNR of the highest harmonic relative to the noise floor after performing an FFT on the TIA output, a sensor DC bias of $E_{1/2}$= 155 mV, and a 40 mV peak-to-peak, 50% duty-cycle square wave (period of 2 s) were applied to the model for three cycles. The $R_f$ was set to 4 MOhm for the worst-case scenario identified previously, and the TIA output was sampled at 2 kHz. The applied signal to the Verilog-A model and the TIA output in time-domain are shown in Fig. 15 (a), and the FFT of the resulting current with non-zero padding is shown in Fig. 15(b), where the SNR between the smallest harmonic at 500 Hz and the noise floor is approximately 28 dB, thereby ensuring accurate detection for the proposed EIS technique.

The stability and bandwidth of the TIA restrict the decision of $C_f$ and $R_f$, and a simplified equivalent model for the stability and bandwidth analysis is shown in Fig. 13(b). The Verilog-A model provides a more realistic sensor behavior for simulations; however, due to the fact the CPE contains a




(a). (b).

Fig. 16. The measurement setup and the die micrograph: (a). The test setup, and (b). the die micrograph.

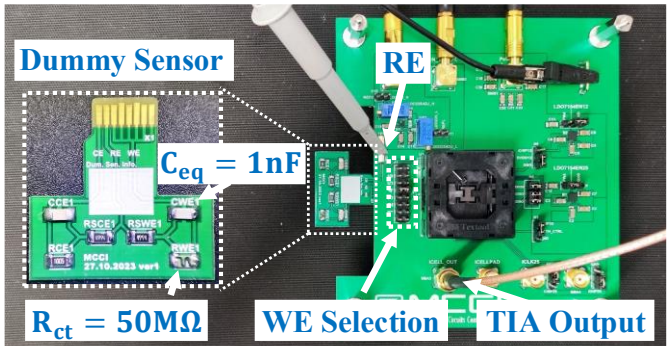



Fig. 17. The PCB setup for electrical validation, with an $R_{ct}$ = 50 MOhm, and a $C_{eq}$ = 1 nF.

fractional term, $(j\omega)^{\gamma}$, no analytical solution in terms of frequency response can be obtained for a straightforward analysis. Therefore, the CPE in circuit analysis calculation is expressed with an equivalent capacitor, $C_{eq}$, aimed to provide an "intuitive" design trade-off.

The loop gain without a compensation capacitor, $LG_{w/o,C_f}$, as described in (21), indicates that two poles located at $1/2\pi R_{out}C_{load}$ and $(1 + R_f/R_{ct})/2\pi R_f C_{eq}$ yield poor stability.

$$LG_{w/o,C_f} = A_v(j\omega)\,\beta(j\omega) = \frac{A_{op}}{(1 + j\omega R_{out}C_{load})} \cdot \frac{1}{\left[\left(1 + \frac{R_f}{R_{ct}}\right) + j\omega R_f C_{eq})\right]} \qquad (21)$$

where $A_{op}(j\omega)$ is the gain of the amplifier, which is designed to be a first-order linear system within the Unit Gain Bandwidth (UGB). $A_{op}$, $R_{out}$ and $C_{load}$ are the DC gain, equivalent output resistance and load capacitance of the amplifier respectively.

It can be seen that the instability occurs at the intercept frequency, $f_{int}$, when $A_v(j\omega) = 1/\beta(j\omega)$, as is expressed in (22), assuming $A_{op}$ is large.

$$f_{int} \approx \frac{1}{2\pi}\sqrt{\frac{A_{op}}{C_{eq}R_f C_{load}R_{out}}} \qquad (22)$$

The compensation capacitor, $C_f$, introduces a zero of $1/2\pi C_f R_f$ for TIA compensation, and the loop gain of the TIA with $C_f$ is expressed with (23):

Authorized licensed use limited to: UNIVERSITY COLLEGE CORK. Downloaded on July 07,2025 at 14:33:53 UTC from IEEE Xplore. Restrictions apply.
© 2025 IEEE. All rights reserved, including rights for text and data mining and training of artificial intelligence and similar technologies. Personal use is permitted, but republication/redistribution requires IEEE permission. See https://www.ieee.org/publications/rights/index.html for more information.

This article has been accepted for publication in IEEE Transactions on Biomedical Circuits and Systems. This is the author's version which has not been fully edited and content may change prior to final publication. Citation information: DOI 10.1109/TBCAS.2025.3579698



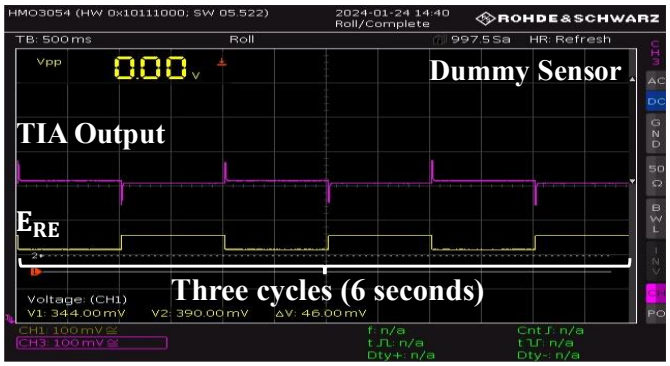



Fig. 18. The time-domain results of the sensor input and TIA output for a dummy sensor, with an $R_{ct}$ = 50 MOhm, and a $C_{eq}$ =1 nF.

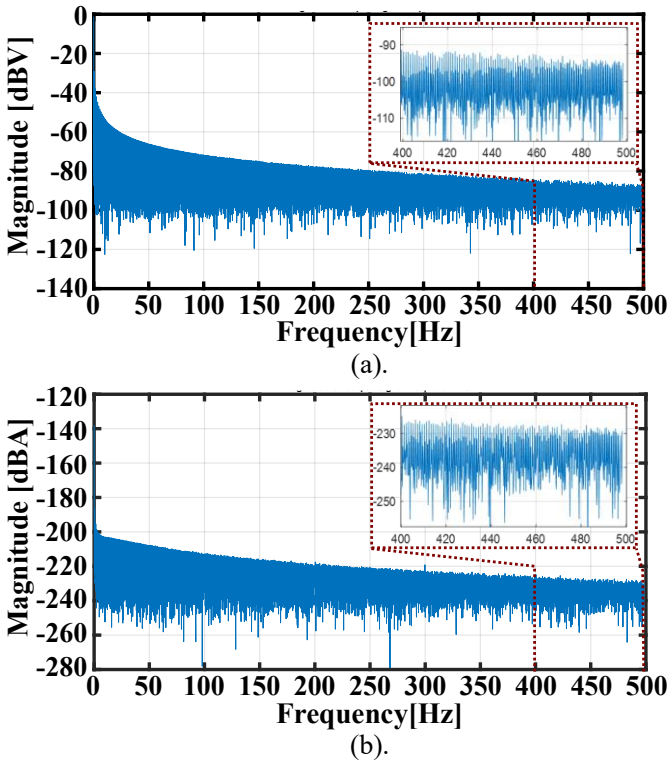



Fig. 19. The FFT results of the measured square-wave EIS with a dummy sensor: (a). the FFT results of the applied potential at RE, and (b). the FFT results of the current converted from TIA output.

$$LG_{w/,C_f} = \frac{A_{op}R_{ct}\left(1+j\omega C_f R_f\right)}{\left(R_f+R_{ct}+j\omega\left(C_f+C_{eq}\right)R_f R_{ct}\right)\left(1+j\omega C_{load}R_{out}\right)}. \quad (23)$$

Consequently, the zero of the TIA should be placed before the intercept frequency $f_{int}$, namely, $1/2\pi C_f < f_{int}$, where the feedback capacitor is thus determined by (24):

$$C_f \geq \sqrt{C_{eq}C_{load}R_{out}/A_{op}R_f}\,. \quad (24)$$

By evaluating the transfer function of the TIA, the 3-dB bandwidth, $f_{3db}$, is obtained by examining its dominant pole, as is expressed in (25), if the TIA is overcompensated.

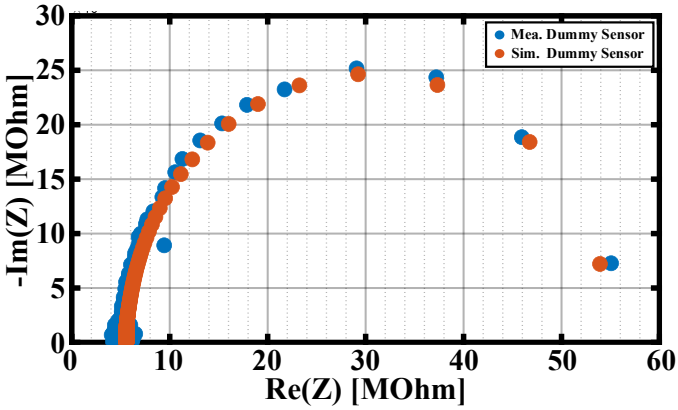



Fig. 20. The chip-tested results of square-wave EIS and simulated results of a dummy sensor, with an $R_{ct}$ = 50 MOhm, and a $C_{eq}$ = 1 nF.

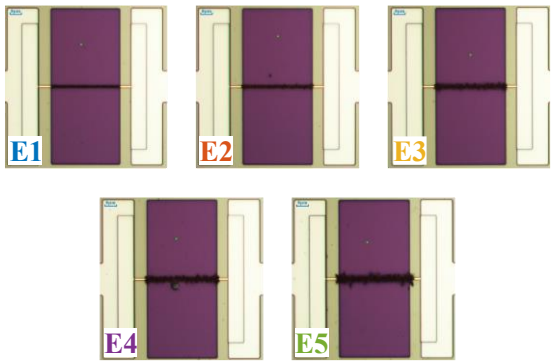



Fig.21. Microscopic images of five electrodes with different deposited thicknesses of gold.

$$f_{3db} \approx \frac{1}{2\pi C_f R_f} \quad (25)$$

In practice, considering variations in the CPE across different chemical tests, $C_f$ should be chosen to exceed $\sqrt{C_{eq}C_{op}R_{op}/A_{op}R_f}$ substantially for overcompensation, and the CPE should be set to a relatively large value when designing circuity with simulations. For UMB electrode sensors, the values of $Q$ and $\gamma$ of CPE are empirically chosen to be 10 $nF$ and 0.8 respectively, and the CPE is approximated in a frequency range of 0.0001 Hz to 1 GHz for stability and bandwidth simulations. It can be observed from (22) and (25) that the sensor small-signal charge-transfer resistance has negligible impact on stability and bandwidth; hence the $R_{ct}$ is fixed at a DC bias of 0.155 V in the Verilog-A model (the middle of the sensor linear region). A stability analysis and an AC small-signal analysis are performed by sweeping $R_f$ from 4 MOhm to 20 MOhm with $C_f$ in a range of 1 pF to 10 pF. The simulated results of transimpedance gain, loop gain, loop phase, amplifier gain, and $1/\beta$ are shown in Fig. 14(b), with an $R_f$ and $C_f$ of 10 MOhm and 5 pF respectively, and a valid bandwidth of 3.3 kHz with overcompensation.

## IV. Experimental Results

The designed chip was fabricated in a 65 nm CMOS technology with an active area of 140 μm × 195 μm. The sensor excitations for both CV and square-wave EIS are

Authorized licensed use limited to: UNIVERSITY COLLEGE CORK. Downloaded on July 07,2025 at 14:33:53 UTC from IEEE Xplore. Restrictions apply.
© 2025 IEEE. All rights reserved, including rights for text and data mining and training of artificial intelligence and similar technologies. Personal use is permitted, but republication/redistribution requires IEEE permission. See https://www.ieee.org/publications/rights/index.html for more information.

This article has been accepted for publication in IEEE Transactions on Biomedical Circuits and Systems. This is the author's version which has not been fully edited and content may change prior to final publication. Citation information: DOI 10.1109/TBCAS.2025.3579698



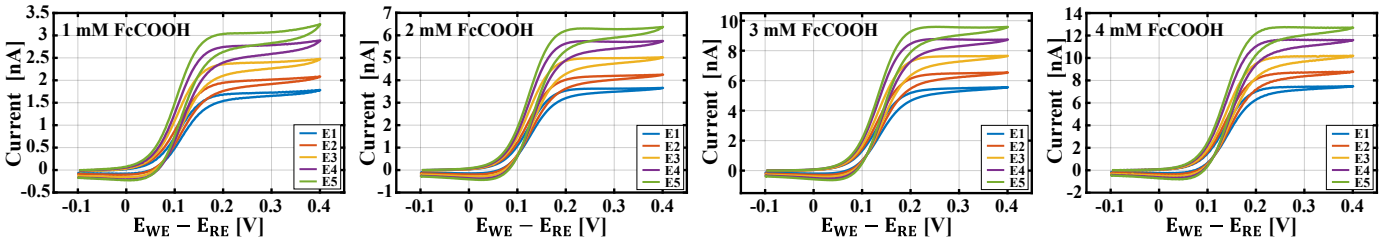



Fig. 22. The CV results performed by AutoLab in (a). 1 mM FcCOOH, (b). 2 mM FcCOOH, (c). 3 mM FcCOOH, and (d). 4 mM FcCOOH, in a 10 mM PBS supporting electrolyte at 25°, with a SR of 50 mV/s from -0.1 V to 0.4 V, showing different electrode characteristics for the electrochemical validation.

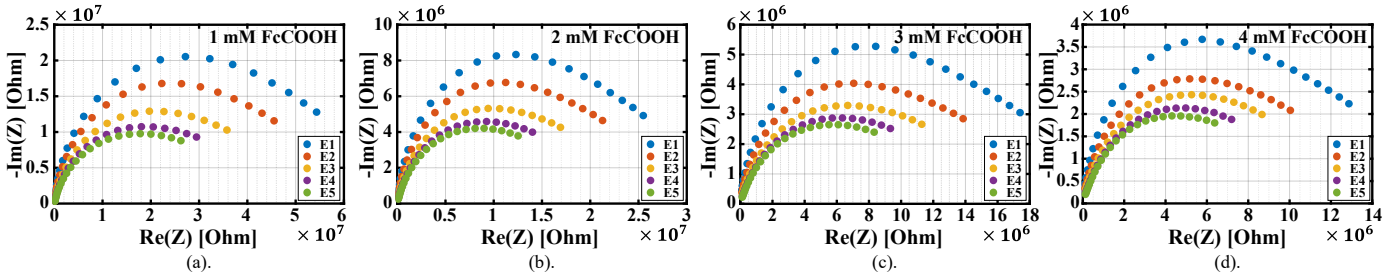



Fig.23. The EIS results performed by AutoLab in (a). 1 mM FcCOOH, (b). 2 mM FcCOOH, (c). 3 mM FcCOOH, and (d). 4 mM FcCOOH, in a 10 mM PBS supporting electrolyte at 25°, with DC at each $E_{1/2}$ and an AC amplitude of 40 mV to validate the deposited electrodes.

.

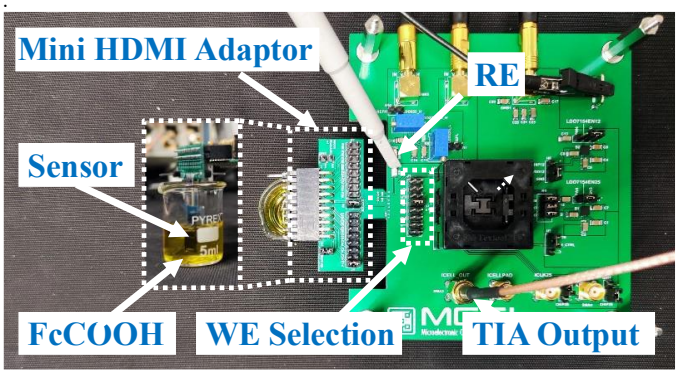



Fig. 24. The PCB setup for chemistry test with deposited UMB electrodes.

generated using a Tektronix AFG1062. The potentials of the RE (as the sensor input) and the TIA output are synchronously sampled by a Rohde & Schwarz HMO3004, serving as an Analog-to-Digital Convertor (ADC). The test setup and the die micrograph are shown in Fig. 16(a) and (b).

### *A. Electrical Validation of the Chip with Dummy Sensor*

Electrical validation of the chip is performed using a dummy sensor, where $R_{ct} = 50$ MOhm (and $C_{eq} = 1$ nF, as is shown in Fig. 17. A 5 MOhm resistor is added in the signal path to prevent the low impedance looking into the dummy sensor. A square wave at a frequency of 0.5 Hz with an AC magnitude of 40 mV is applied to the dummy sensor via a function generator Tektronix AFG1062, and the signals at the RE and TIA output are sampled via Rohde & Schwarz HMO3004 at a sampling rate of 1 kHz. The dummy sensor current, $I_{dum}$, is given by (26):

$$I_{dum}(t) = -\frac{V_{TIA,out}(t)}{R_f} + \frac{V_{CM,TIA}}{R_f} \tag{26}$$

where $V_{TIA,out}(t)$ is the TIA output and $V_{CM,TIA}$ is the TIA common-mode DC level.

Fig. 18 shows the time-domain sampled input and output signals, and Fig. 19 (a) shows the FFT results of the applied potential at RE, and Fig. 19(b) shows the FFT results of the TIA output. Fig. 20 compares the dummy sensor's square-wave-based EIS measurement results with simulated EIS data. It can be observed that the highest frequency harmonic is at 500 Hz, with a magnitude -230 dBA of the sensor output, and a magnitude of -95 dBV of the applied potential. At higher frequency, the SNR becomes worse due to the decreasing amplitude of the square wave harmonics, while the close agreement between the tested EIS and simulated EIS confirms that the designed potentiostat and TIA satisfy the expected bandwidth, noise, and stability requirements, but limits the frequency band to 500 Hz as target.

### *B. The Pre-modification of the UMB Electrodes*

Five pre-modified WEs, denoted as E1 to E5, featuring progressively thicker gold deposits that decrease $R_{ct}$ while increasing the CPE, are tested across 1 mM to 4 mM concentrations of FcCOOH at room temperature for validating the feasibility of the proposed square-wave EIS for biomedical applications.

The pre-modification of the electrode involves the deposition of gold (Au) onto the electrode surface, which yields different characteristics for both the CPE and $R_{ct}$. The deposition occurs in the solution dissolving 5 mM $HAuCl_3$ in 0.25 M $H_2SO_4$ at 25°. The chemical formula of this reaction is described by (27):

$$Au^{2+} + 2e^- \rightarrow Au. \tag{27}$$

The deposition is done with Chronoamperometry based on AutoLab, where the thickness is controlled by the deposition duration with a given fixed electrode potential (-0.1V this case). In this test, five UMB electrodes, designated E1 to E5, are deposited with five different durations: 4s, 8s, 10s, 14s and 18s, respectively. The microscopic images of the electrodes, E1 to E5, after the deposition are depicted in Fig. 21.

CV and EIS are then conducted using AutoLab to inspect the

Authorized licensed use limited to: UNIVERSITY COLLEGE CORK. Downloaded on July 07,2025 at 14:33:53 UTC from IEEE Xplore. Restrictions apply.
© 2025 IEEE. All rights reserved, including rights for text and data mining and training of artificial intelligence and similar technologies. Personal use is permitted, but republication/redistribution requires IEEE permission. See https://www.ieee.org/publications/rights/index.html for more information.

This article has been accepted for publication in IEEE Transactions on Biomedical Circuits and Systems. This is the author's version which has not been fully edited and content may change prior to final publication. Citation information: DOI 10.1109/TBCAS.2025.3579698



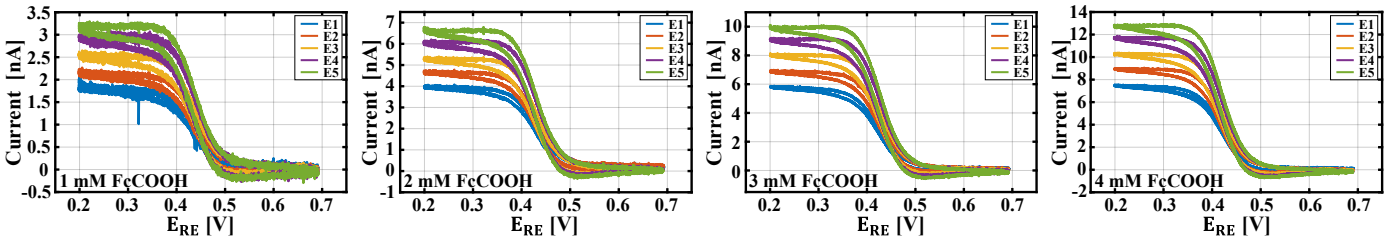



Fig. 25. The chip-tested results of CV across (a). 1 mM FcCOOH, (b). 2 mM FcCOOH, (c). 3 mM FcCOOH, and (d). 4 mM FcCOOH, in a 10 mM PBS supporting electrolyte at 25°, with a SR of 50 mV/s for electrode potential from -0.1 V to 0.4 V. The results shows that the UMB sensor is working as expected.

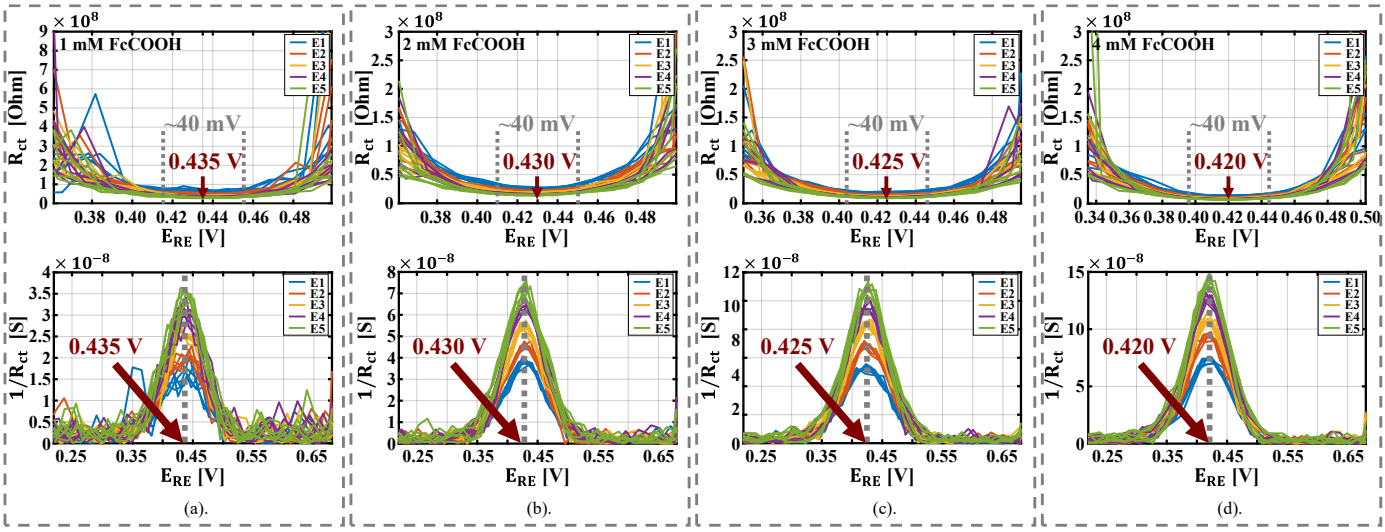



Fig. 26. The determination of AC and DC conditions for square-wave EIS across (a). 1 mM FcCOOH, (b). 2 mM FcCOOH, (c). 3 mM FcCOOH, and (d). 4 mM FcCOOH, in a 10 mM PBS supporting electrolyte at 25°. The DC bias of the sensor is chosen where the conductance of the sensor reaches minimum, namely, the half potential, and the AC amplitude is chosen to be 40 mV as mentioned in Section II, where the sensor working in a linear region.

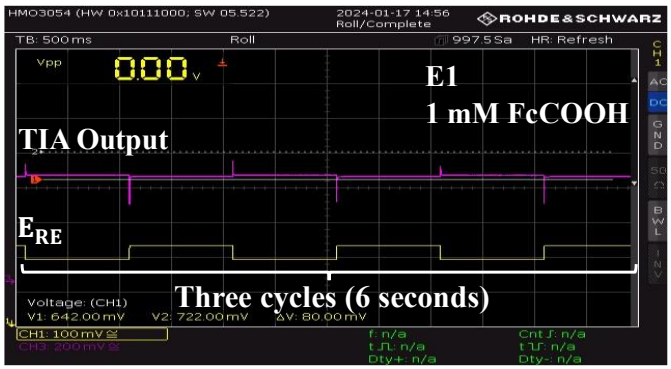



Fig. 27. The time-domain results of the sensor input and TIA output for E1.

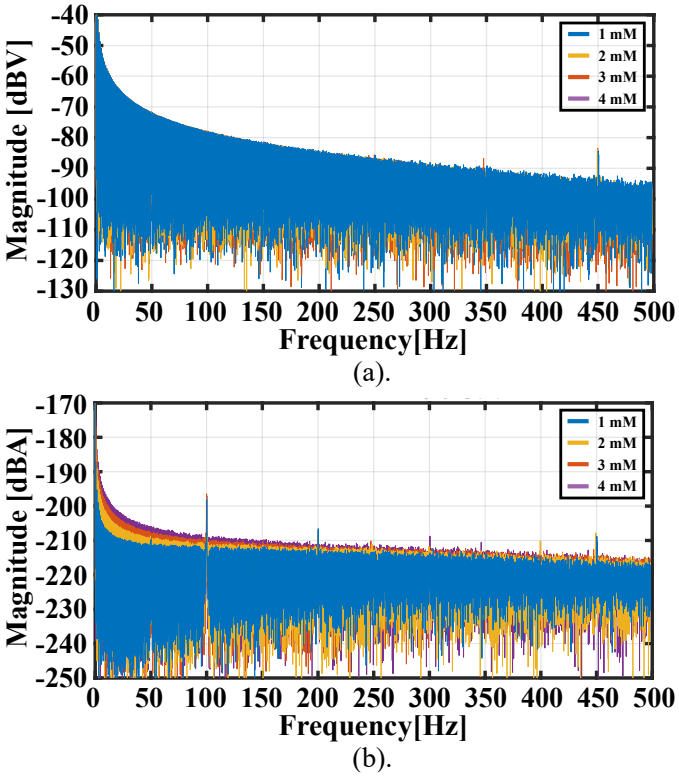



Fig. 28. The FFT results of the chip-measured square-wave EIS with E1 in 1 - 4 mM FcCOOH: (a). the FFT results of the applied potential at RE, and (b). the FFT results of the current converted from the TIA output

performance of the deposited UMB electrodes. Fig. 22(a) to (d) show the CV results of each deposited electrode across 1 mM to 4 mM concentrations of FcCOOH in a 10 mM PBS supporting electrolyte at 25°, with a SR of 50 mV/s from -0.1 V to 0.4 V, and the EIS measurement results with DC at each $E_{1/2}$ are shown from Fig. 23(a) to (d). It can be seen that after doing the deposition, five electrodes show different characteristics in different concentrations of FcCOOH, which can be used to conduct the electrochemical validation.

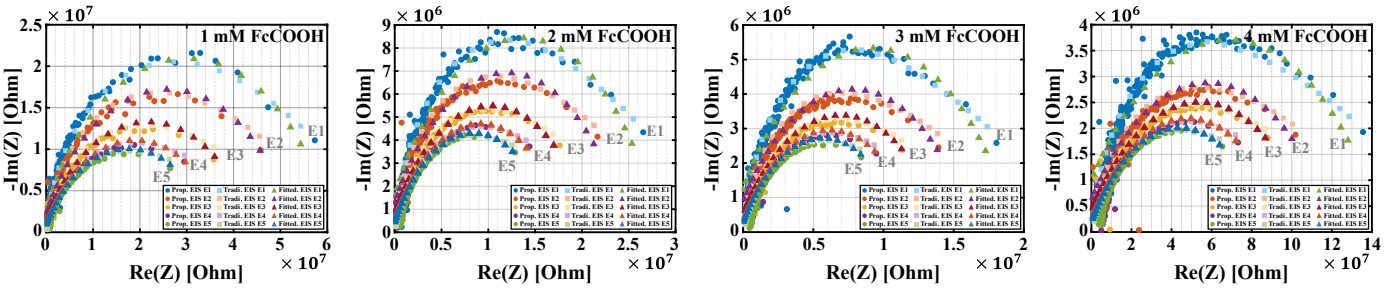
### *C. Electrochemical Validation of the Proposed Square-wave EIS with Pre-deposited UMB Electrodes*

The test setup for the electrochemical validation of the proposed square-wave EIS is shown in Fig. 24. The sensor

Authorized licensed use limited to: UNIVERSITY COLLEGE CORK. Downloaded on July 07,2025 at 14:33:53 UTC from IEEE Xplore. Restrictions apply.
© 2025 IEEE. All rights reserved, including rights for text and data mining and training of artificial intelligence and similar technologies. Personal use is permitted, but republication/redistribution requires IEEE permission. See https://www.ieee.org/publications/rights/index.html for more information.

This article has been accepted for publication in IEEE Transactions on Biomedical Circuits and Systems. This is the author's version which has not been fully edited and content may change prior to final publication. Citation information: DOI 10.1109/TBCAS.2025.3579698






(a). (b). (c). (d).

Fig. 29. The comparison of EIS results of the square wave EIS, the traditional EIS performed by AutoLab, and the EIS optimized fitted model.

TABLE IV. ERROR EVALUATION

| | | MAPE1 (%) | MAPE2 (%) | Error (%) |
|---|---|---|---|---|
| **1mM** | E1 | 13.27 | 10.95 | 2.32 |
| | E2 | 13.47 | 13.49 | 0.02 |
| | E3 | 11.31 | 10.82 | 0.49 |
| | E4 | 10.44 | 13.23 | 2.79 |
| | E5 | 9.60 | 9.20 | 0.40 |
| | | **1 mM Ave.** | | **1.20** |
| **2mM** | E1 | 11.35 | 15.26 | 3.91 |
| | E2 | 10.87 | 13.05 | 2.18 |
| | E3 | 8.52 | 9.41 | 0.89 |
| | E4 | 7.09 | 8.33 | 1.24 |
| | E5 | 6.52 | 8.84 | 2.32 |
| | | **2 mM Ave.** | | **2.11** |
| **3mM** | E1 | 9.79 | 16.25 | 6.46 |
| | E2 | 8.71 | 7.57 | 1.14 |
| | E3 | 5.88 | 8.91 | 3.03 |
| | E4 | 4.85 | 10.40 | 5.55 |
| | E5 | 4.53 | 9.81 | 5.28 |
| | | **3 mM Ave.** | | **4.29** |
| **4mM** | E1 | 8.46 | 13.42 | 4.96 |
| | E2 | 7.20 | 7.98 | 0.78 |
| | E3 | 4.74 | 7.38 | 2.64 |
| | E4 | 3.64 | 7.44 | 3.80 |
| | E5 | 3.54 | 7.99 | 4.45 |
| | | **4 mM Ave.** | | **3.33** |
| | | **Total Ave.** | | **2.73** |

communicates with the designed chip through a Micro-SD-to-Mini-HDMI PCB adaptor.

In the measurement of CV, a triangle wave at a frequency of 0.05 Hz is applied, which ensures the potential of the WE has a scan rate of 50 mV/s sweeping from -0.1 V to 0.4 V with respect to the TIA common mode potential, 0.6 V. The chip-tested results of CV across 1 mM to 4 mM FcCOOH are shown from Fig. 25(a) to (d), and the DC bias of the sensor is chosen where the conductance of the sensor reaches minimum, namely, the half potential, and the AC amplitude is chosen to be 40 mV as mentioned in Section II, where the sensor works in a linear region, as shown in Fig. 26(a) to (d).

The frequency of the square wave for EIS is chosen to be 0.5 Hz, and the input and output are sampled for three cycles with a sampling rate of 1,000 samples per second for a Nyquist bandwidth of 500 Hz. The time-domain chip-tested results of E1 in 1 mM FcCOOH are shown in Fig. 27, and FFT results of E1 in 1-4 mM FcCOOH are shown in Fig. 28, then the same measurement is repeated for the remaining electrodes and concentrations. It can be seen that, for the E1 in 1 mM FcCOOH, the highest frequency harmonic is at 500 Hz, with a magnitude -218 dBA of the sensor output, and a magnitude of -95 dBV of the applied potential. Fig. 29(a) to (d) compare the tested square wave EIS, the traditional EIS from Autolab, and the fitted EIS model for five electrodes across four FcCOOH concentrations. The optimized fitted EIS model is obtained using AutoLab based on the traditional EIS.

It can be seen that the proposed chip-tested square wave EIS has high consistency with the traditional EIS based on AutoLab, while only consuming 6 seconds, shortened by 91.7% from 72 seconds in a conventional way [57].

### *D. Error Evaluation*

The error was investigated by comparing the absolute difference between the MAPE of traditional EIS and the model fitted using traditional EIS data, against the MAPE between square wave EIS and the model fitted using traditional EIS, as expressed in (28):

$$Error = \left| \underbrace{\frac{1}{m}\sum_{i=1}^{m}\left|\frac{Z_{i,fit.} - Z_{i,mea.}}{Z_{i,fit.}}\right|}_{\substack{\text{MAPE1:}\\ \text{Traditional EIS vs. fitted model}}} - \underbrace{\frac{1}{n}\sum_{j=1}^{n}\left|\frac{Z_{j,fit.} - Z_{j,mea.}}{Z_{j,fit.}}\right|}_{\substack{\text{MAPE2:}\\ \text{Proposed EIS vs. fitted model}}} \right| \cdot 100\% \quad (28)$$

where $m$ and $n$ are the number of the frequencies in traditional EIS data and square wave EIS data, respectively. $Z_{i,mea.}$ and $Z_{j,mea.}$ represent the measured impedance magnitudes of the traditional EIS and square wave EIS, respectively, where $i \in [1, m]$ and $j \in [1, n]$ are integer numbers. $Z_{i,fit}$ and $Z_{j,fit}$ represent the calculated impedance magnitudes from the optimized fitted EIS model. The calculated errors are listed in Table IV.

It can be seen that the average MAPE between chip-tested square-wave EIS and the traditional EIS conducted by the commercial instrument AutoLab is 2.73%, and the measurement time is reduced by 91.7% (from 72 seconds to 6 seconds), 12 times faster than single frequency sweep. Compare to other relevant published works shown in Table V, the proposed square wave EIS shows fair competitive coherency and accuracy but much less measurement time. These tested results successfully validate the feasibility for applying the proposed square-wave EIS technique to portable, real-time

Authorized licensed use limited to: UNIVERSITY COLLEGE CORK. Downloaded on July 07,2025 at 14:33:53 UTC from IEEE Xplore. Restrictions apply.
© 2025 IEEE. All rights reserved, including rights for text and data mining and training of artificial intelligence and similar technologies. Personal use is permitted, but republication/redistribution requires IEEE permission. See https://www.ieee.org/publications/rights/index.html for more information.

This article has been accepted for publication in IEEE Transactions on Biomedical Circuits and Systems. This is the author's version which has not been fully edited and content may change prior to final publication. Citation information: DOI 10.1109/TBCAS.2025.3579698



TABLE V. COMPARISON WITH RELEVANT PUBLISHED WORKS

| | [14] | [15] | [17] | [18] | [19] | [20] | [22] | [24] | [25] | [31] | [32] | [33] | [34] | This work |
|---|---|---|---|---|---|---|---|---|---|---|---|---|---|---|
| **Technology** | 0.13 µm | 0.5 µm | 130 nm | 180 nm | 0.35 µm | N/A | N/A | N/A | N/A | 40 nm | N/A | N/A | 0.11 µm | **65 nm** |
| **Supply Voltage** | 1.2 V | 3 V | 0.6 V | 1.8 V | 3.3 V | N/A | N/A | N/A | N/A | 0.9 V | N/A | N/A | 1.2 V | **2.5 V** |
| **Power** | 0.35 mW | 6 µW | 14.6 µW | 344.3 µW to 479.3 µW | 0.32 mW | N/A | N/A | N/A | N/A | 135 µW | N/A | 14.4 mW | 1.28 mW | **1.25 mW / Amplifier** |
| **Core Area** | 1.68 mm² | 0.06 mm² | 0.004 mm² | 5.4 mm² | 0.07 mm² | N/A | N/A | N/A | N/A | 0.6 mm² | N/A | N/A | 6 mm² | **0.027 mm²** |
| **Excitation Type** | Sinusoidal | Sinusoidal | Sinusoidal | Sinusoidal | Sinusoidal | Multi-sine Excitation | Chirp signals | Structured Gaussian White Noise | Pseudo-Random Binary Sequence | Square-wave (i) | Square-wave (i) | Square-wave (i) | Square-wave (i) | **Square-wave (v)** |
| **Signal Generation** | On-chip 8-bit R-2R DAC and SRAM | External Signal Generator | External Signal Generator | On-chip Direct Digital-Synthesis | External Signal Generator | External Signal Generator | External Signal Generator | External Signal Generator | External Signal Generator | External Signal Generator | External Signal Generator | External Signal Generator | On-Chip Switched Current Stimulus | **1-bit DAC (External Signal Generator)** |
| **Chemical Verification** | Yes (Potassium Ferricyanide DNA) | Yes (Protein) | Yes (Potassium) | Yes (Biological Tissue) | Yes (ZoBell's ORP/redox Standard Solution and Melatonin Solutions) | Yes (18650-29E Battery) | Yes (Sealed Lead Acid battery and Lithium Nickel-Cobalt Anganese Oxide) | No | Yes (Lithium-iron-phosphate and Battery cell) | Yes (Biological Tissue) | Yes (Biological Tissue) | Yes (Biological Tissue) | Yes (Biological Tissue) | **Yes (Ferrocene Carboxylic Acid)** |
| **Measurement Time** | N/A | N/A | N/A | N/A | N/A | N/A | 5-12 times faster than single-sine frequency sweep | **6.08 times faster than single-sine frequency sweep** | **12 times faster than single-sine frequency sweep** | N/A | N/A | N/A | N/A | **12 times faster than single-sine frequency sweep** |
| **Error** | **8.4% (Real) 7.5% (Imag) (Relative Error, Impedance Model)** | N/A | < 2% | < 3% | 0.28% (Mag., 10 kHz) 0.12% (Pha., 10 Hz) (RMS Error) | < 4.5% | N/A | **< 2.69% (Relative Error)** | **< 8.3% (RMS)** | N/A | < 1% (Mag.) < 0.5° (Pha.) | 7.2% | N/A | **2.73% (MAPE)** |

label-free impedance-based biomedical applications

## V. DISCUSSION

### *A. The Applicability of the Proposed Square Wave-based EIS.*

The accuracy and feasibility of the proposed square wave-based EIS for biomedical applications are validated with UMB electrode sensors, whose charge-transfer rate model can be described with Butler Volmer relationships theoretically, owing to its highly efficient three-dimensional mass diffusion mechanism. In the case of an UMB electrode sensor, a linear region is determined, which provides the applicability of this technique. Based on this fact, it can be inferred that other types of micro electrodes that have highly efficient radial mass diffusion transportation, such as micro disk electrodes, can potentially use this technique for performing EIS. However, due to the different electrode shapes, a different charge-transfer rate model should be proposed and validated [40], and further chemical tests would need to be followed. The proposed square-wave EIS provides a new angle to develop new techniques and circuits for conducting fast, and high-accurate EIS with UMB electrode sensors, particularly, for sensor-on-chip and implantable biomedical applications [39, 58–62].

The limited frequency range restricts this technique for a wider application; however, depending on the application, by applying square waves with different frequencies, the frequency range can be extended to enhance spectral coverage. Apart from that, different excitation signals such as a duty-cycle controlled square wave potentially can provide more harmonic tones for a wider application. The AC amplitude used in this work with a UMB sensor is 40 mV, where the sensor shows linearity. Due to the fact that this type of sensor, whose mass transport is dominated by a radical diffusion, the $R_{ct}$ can be fitted with (9); therefore, the 40 mV should be applicable as well. However, like a normal EIS measurement, a CV should be conducted before the EIS test, to find the AC and DC conditions practically, and in order to accommodate different sensors, strategies to optimize the AC amplitude can be investigated further.

### *B. The Impact of the Proposed Verilog-A model.*

Owing to the fact that the UMB sensor behavior, namely, the relation between the electrode potential and sensor current, sensor transconductance and impedance, double-layer effect (CPE), etc., are mathematically modeled, a dynamic Verilog-A model is implemented and utilized in this work. This dynamic model has advantages in accuracy and convenience in terms of the bandwidth and stability analysis, as well as the transient analysis, for designing different potentiostats, such as control amplifier-based potentiostat [63–65], current-mirror-based potentiostat [66], Delta-sigma modulation potentiostat [67, 68], Amplifier-less potentiostat [69, 70], etc., and current readout ICs of UMB electrochemical sensors.

### *C. The Required Specification of the Amplifier and TIA.*

The loop gain and its bandwidth are dominated by the pole of the amplifier, and the pole introduced by a low-pass filter formed by the CPE and the feedback network, as described in (21). It indicates that a larger electrode active surface, or a higher concentration of the solution may attenuate the loop gain at high-frequency harmonics and cause instability, which ultimately results in errors at the TIA output. Therefore, when applying this technique, the amplifier should be designed to have low-noise and a high bandwidth, in order to compensate the attenuated loop gain and bandwidth at higher frequencies caused by the varying CPE and the overcompensation of the TIA. This proposes the challenges in amplifier design techniques. In addition, this work is aimed to validate the proposed square wave EIS; therefore, the power consumption was not considered. However, in the practical application, the power of the amplifier should be optimized.

## VI. CONCLUSION

This work demonstrates a square wave-based EIS method with the advantages of simplicity of implementation and fast measurement time. The theories under which the sensor is linearized as an LTI system lay the groundwork for using square wave as the EIS excitation signal, also potentially

Authorized licensed use limited to: UNIVERSITY COLLEGE CORK. Downloaded on July 07,2025 at 14:33:53 UTC from IEEE Xplore. Restrictions apply.
© 2025 IEEE. All rights reserved, including rights for text and data mining and training of artificial intelligence and similar technologies. Personal use is permitted, but republication/redistribution requires IEEE permission. See https://www.ieee.org/publications/rights/index.html for more information.

This article has been accepted for publication in IEEE Transactions on Biomedical Circuits and Systems. This is the author's version which has not been fully edited and content may change prior to final publication. Citation information: DOI 10.1109/TBCAS.2025.3579698



bringing opportunities for novel EIS circuitry. The successful validation of the proposed EIS on a taped-out chip yields an average MAPE of 2.73%, compared to the results from a commercial instrument, while the measurement time is shortened to 6 seconds from 72 seconds, by 91.7%, in a frequency range of 0.5 Hz to 500 Hz. The high accuracy and fast measurement time ensure the feasibility for applying this technique to portable, real-time impedance-based biomedical applications.

## VII. Reference

[1] J. Wang, "Electrochemical Sensing of Explosives," *Electroanalysis*, vol. 19, no. 4, pp. 415–423, 2007, doi: 10.1002/elan.200603748.

[2] J. Baranwal, B. Barse, G. Gatto, G. Broncova, and A. Kumar, "Electrochemical Sensors and Their Applications: A Review," *Chemosensors*, vol. 10, no. 9, p. 363, 2022, doi: 10.3390/chemosensors10090363.

[3] N. T. Kemp, "A Tutorial on Electrochemical Impedance Spectroscopy and Nanogap Electrodes for Biosensing Applications," *IEEE Sensors J.*, vol. 21, no. 20, pp. 22232–22245, 2021, doi: 10.1109/JSEN.2021.3084284.

[4] Q. Zhu *et al.,* "Electrochemical preparation of polyaniline capped Bi2S3 nanocomposite and its application in impedimetric DNA biosensor," *Sensors and Actuators B: Chemical*, vol. 207, pp. 819–826, 2015, doi: 10.1016/j.snb.2014.10.120.

[5] N. Creedon, R. sayers, B. O'sullivan, e. kennedy, P. Lovera, and A. O'Riordan, *Label-Free Impedimetric Nanoband Sensor for Detection of Both Bovine Viral Diarrhoea Virus (BVDV) and Antibody (BVDAb) in Serum*, 2018.

[6] W. M. Hassen, V. Duplan, E. Frost, and J. J. Dubowski, "Quantitation of influenza A virus in the presence of extraneous protein using electrochemical impedance spectroscopy," *Electrochimica Acta*, vol. 56, no. 24, pp. 8325–8328, 2011, doi: 10.1016/j.electacta.2011.07.009.

[7] K. M. Al-Qaoud *et al.,* "The development of an electrochemical immunosensor utilizing chicken IgY anti-spike antibody for the detection of SARS-CoV-2," *Scientific reports*, vol. 14, no. 1, p. 748, 2024, doi: 10.1038/s41598-023-50501-w.

[8] R. K. Shervedani, A. H. Mehrjardi, and N. Zamiri, "A novel method for glucose determination based on electrochemical impedance spectroscopy using glucose oxidase self-assembled biosensor," *Bioelectrochemistry (Amsterdam, Netherlands)*, vol. 69, no. 2, pp. 201–208, 2006, doi: 10.1016/j.bioelechem.2006.01.003.

[9] D. M. G. Preethichandra and P. Sonar, "Electrochemical Impedance Spectroscopy and its Applications in Sensor Development and Measuring Battery Performance," *IEEE Sensors J.*, vol. 22, no. 11, pp. 10152–10162, 2022, doi: 10.1109/JSEN.2021.3119650.

[10] I. Mostafa and R. Brederlow, "Trends, Challenges, and Recent Advances in Electrochemical Impedance Spectroscopy," *IEEE Sens. Lett.*, vol. 6, no. 5, pp. 1–4, 2022, doi: 10.1109/LSENS.2022.3162773.

[11] A. C. Lazanas and M. I. Prodromidis, "Electrochemical Impedance Spectroscopy-A Tutorial," *ACS measurement science au*, vol. 3, no. 3, pp. 162–193, 2023, doi: 10.1021/acsmeasuresciau.2c00070.

[12] Z. Lu *et al.,* "A point of care electrochemical impedance spectroscopy device," in *2015 28th IEEE International System-on-Chip Conference (SOCC)*, Beijing, China, 2015, pp. 240–244.

[13] Y.-R. Wang, S. C. Chien, Y. C. Lin, and J.-C. Chen, "Portable Electrochemical Impedance Spectroscopy Device Implementation for Alzheimer's Disease-Related Protein," *Meet. Abstr.*, MA2023-01, no. 34, p. 1892, 2023, doi: 10.1149/MA2023-01341892mtgabs.

[14] *AD5933 Datasheet and Product Info | Analog Devices.* [Online]. Available: https://www.analog.com/en/products/ad5933.html (accessed: Mar. 21 2025).

[15] C. Yang, S. R. Jadhav, R. M. Worden, and A. J. Mason, "Compact Low-Power Impedance-to-Digital Converter for Sensor Array Microsystems," *IEEE J. Solid-State Circuits*, vol. 44, no. 10, pp. 2844–2855, 2009, doi: 10.1109/JSSC.2009.2028054.

[16] H. Mazhab-Jafari, L. Soleymani, and R. Genov, "16-channel CMOS impedance spectroscopy DNA analyzer with dual-slope multiplying ADCs," *IEEE transactions on biomedical circuits and systems*, vol. 6, no. 5, pp. 468–478, 2012, doi: 10.1109/TBCAS.2012.2226334.

[17] M. ElAnsary *et al.,* "50nW Opamp-Less ΔΣ-Modulated Bioimpedance Spectrum Analyzer for Electrochemical Brain Interfacing," *IEEE J. Solid-State Circuits*, vol. 55, no. 7, pp. 1971–1983, 2020, doi: 10.1109/JSSC.2020.2981033.

[18] A. D. F. Schrunder, Y.-K. Huang, S. Rodriguez, and A. Rusu, "A Bioimpedance Spectroscopy Interface for EIM Based on IF-Sampling and Pseudo 2-Path SC Bandpass ΔΣ ADC," *IEEE Trans. Biomed. Circuits Syst.*, vol. 18, no. 5, pp. 1001–1013, 2024, doi: 10.1109/TBCAS.2024.3370399.

[19] T.-A. Chen, W.-J. Wu, C.-L. Wei, R. B. Darling, and B.-D. Liu, "Novel 10-Bit Impedance-to-Digital Converter for Electrochemical Impedance Spectroscopy Measurements," *IEEE transactions on biomedical circuits and systems*, vol. 11, no. 2, pp. 370–379, 2017, doi: 10.1109/TBCAS.2016.2592511.

[20] X. Wang *et al.,* "Online Detection of Lithium Plating Onset for Lithium-Ion Batteries Based on Impedance Changing Trend Identification During Charging Processes," *IEEE Trans. Transp. Electrific.*, vol. 9, no. 2, pp. 3487–3497, 2023, doi: 10.1109/TTE.2022.3224965.

[21] A. de Angelis, E. Buchicchio, F. Santoni, A. Moschitta, and P. Carbone, "Uncertainty Characterization of a Practical System for Broadband Measurement of Battery EIS," *IEEE Trans. Instrum. Meas.*, vol. 71, pp. 1–9, 2022, doi: 10.1109/TIM.2022.3156994.

[22] O. Alao and P. Barendse, "Online Condition Monitoring of Sealed Lead Acid & Lithium Nickel-Cobalt-Manganese Oxide Batteries using Broadband Impedance Spectroscopy," in *2018 IEEE Energy Conversion Congress and Exposition (ECCE)*, Portland, OR, USA, 2018, pp. 2026–2032.

[23] R. S. Robinson, "System noise as a signal source for impedance measurements on batteries connected to operating equipment," *Journal of Power Sources*, vol. 42, no. 3, pp. 381–388, 1993, doi: 10.1016/0378-7753(93)90005-L.

[24] S. Majzoub, A. Allagui, and A. S. Elwakil, "Fast Spectral Impedance Measurement Method Using a Structured Random Excitation," *IEEE Sensors J.*, vol. 20, no. 15, pp. 8637–8642, 2020, doi: 10.1109/JSEN.2020.2984005.

[25] J. Sihvo, D.-I. Stroe, T. Messo, and T. Roinila, "Fast Approach for Battery Impedance Identification Using Pseudo-Random Sequence Signals," *IEEE Trans. Power Electron.*, vol. 35, no. 3, pp. 2548–2557, 2020, doi: 10.1109/TPEL.2019.2924286.

[26] J. A. A. Qahouq and Z. Xia, "Single-Perturbation-Cycle Online Battery Impedance Spectrum Measurement Method With Closed-Loop Control of Power Converter," *IEEE Trans. Ind. Electron.*, vol. 64, no. 9, pp. 7019–7029, 2017, doi: 10.1109/TIE.2017.2686324.

[27] S.-J. Kweon, A. K. Rafi, S.-I. Cheon, M. Je, and S. Ha, "On-Chip Sinusoidal Signal Generators for Electrical Impedance Spectroscopy: Methodological Review," *IEEE transactions on biomedical circuits and systems*, vol. 16, no. 3, pp. 337–360, 2022, doi: 10.1109/TBCAS.2022.3171163.

[28] S.-I. Cheon *et al.,* "Impedance-Readout Integrated Circuits for Electrical Impedance Spectroscopy: Methodological Review," *IEEE Trans. Biomed. Circuits Syst.*, vol. 18, no. 1, pp. 215–232, 2024, doi: 10.1109/TBCAS.2023.3319212.

[29] C. S. Park, H. Kim, K. Lee, D. S. Keum, D. P. Jang, and J. J. Kim, "A Baseline-Tracking Single-Channel I/Q Impedance Plethysmogram IC for Neckband-Based Blood Pressure and Cardiovascular Monitoring," *IEEE J. Solid-State Circuits*, vol. 58, no. 7, pp. 2040–2052, 2023, doi: 10.1109/JSSC.2022.3221478.

[30] H. Ha *et al.,* "A Bio-Impedance Readout IC With Digital-Assisted Baseline Cancellation for Two-Electrode Measurement," *IEEE J. Solid-State Circuits*, vol. 54, no. 11, pp. 2969–2979, 2019, doi: 10.1109/JSSC.2019.2939077.

[31] T.-T. Zhang, H. Son, J. Zhao, C.-H. Heng, and Y. Gao, "A 26.6–119.3-μW 101.9-dB SNR Direct Digitization Bio-Impedance Readout IC," *IEEE J. Solid-State Circuits*, vol. 58, no. 9, pp. 2619–2631, 2023, doi: 10.1109/JSSC.2023.3269671.

[32] S. Subhan and S. Ha, "A Harmonic Error Cancellation Method for Accurate Clock-Based Electrochemical Impedance Spectroscopy," *IEEE Trans. Biomed. Circuits Syst.*, vol. 13, no. 4, pp. 710–724, 2019, doi: 10.1109/TBCAS.2019.2923719.

[33] S. Lee *et al.,* "A Low-power and Compact-sized Wearable Bio-impedance Monitor with Wireless Connectivity," *J. Phys.: Conf. Ser.*, vol. 434, p. 12013, 2013, doi: 10.1088/1742-6596/434/1/012013.

[34] W. Lee and S. Cho, "Integrated All Electrical Pulse Wave Velocity and Respiration Sensors Using Bio-Impedance," *IEEE J. Solid-State*

Authorized licensed use limited to: UNIVERSITY COLLEGE CORK. Downloaded on July 07,2025 at 14:33:53 UTC from IEEE Xplore. Restrictions apply.
© 2025 IEEE. All rights reserved, including rights for text and data mining and training of artificial intelligence and similar technologies. Personal use is permitted, but republication/redistribution requires IEEE permission. See https://www.ieee.org/publications/rights/index.html for more information.

This article has been accepted for publication in IEEE Transactions on Biomedical Circuits and Systems. This is the author's version which has not been fully edited and content may change prior to final publication. Citation information: DOI 10.1109/TBCAS.2025.3579698



*Circuits*, vol. 50, no. 3, pp. 776–785, 2015, doi: 10.1109/JSSC.2014.2380781.

[35] H. YAMADA, K. YOSHII, M. ASAHI, M. CHIKU, and Y. KITAZUMI, "Cyclic Voltammetry Part 2: Surface Adsorption, Electric Double Layer, and Diffusion Layer," *Electrochemistry*, vol. 90, no. 10, p. 102006, 2022, doi: 10.5796/electrochemistry.22-66084.

[36] I. Jiménez, C. Pérez-Ràfols, N. Serrano, M. Del Valle, and J. Manuel Díaz-Cruz, "Carbon based electrodes for the voltammetric determination of capsaicin in spicy samples," *Microchemical Journal*, vol. 191, p. 108757, 2023, doi: 10.1016/j.microc.2023.108757.

[37] N. Elgrishi, K. J. Rountree, B. D. McCarthy, E. S. Rountree, T. T. Eisenhart, and J. L. Dempsey, "A Practical Beginner's Guide to Cyclic Voltammetry," *J. Chem. Educ.*, vol. 95, no. 2, pp. 197–206, 2018, doi: 10.1021/acs.jchemed.7b00361.

[38] A. Wahl, K. Dawson, J. MacHale, S. Barry, A. J. Quinn, and A. O'Riordan, "Gold nanowire electrodes in array: simulation study and experiments," *Faraday discussions*, vol. 164, pp. 377–390, 2013, doi: 10.1039/C3FD00025G.

[39] H. Jiang, X. Zhou, S. Kulkarni, M. Uranian, R. Seenivasan, and D. A. Hall, "A Sub-1 µW multiparameter injectable BioMote for continuous alcohol monitoring," in *2018 IEEE Custom Integrated Circuits Conference (CICC)*, San Diego, CA, 2018, pp. 1–4.

[40] P. Vanýsek, *Modern techniques in electroanalysis*. New York: Wiley, 1996.

[41] A. J. Bard and L. R. Faulkner, *Electrochemical methods: Fundamentals and applications / Allen J. Bard, Larry R. Faulkner,* 2nd ed. New York, Chichester: John Wiley, 2000.

[42] M. J. A. Shiddiky, A. A. J. Torriero, J. M. Reyna-González, and A. M. Bond, "Nonadditivity of faradaic currents and modification of double layer capacitance in the voltammetry of mixtures of ferrocene and ferrocenium salts in ionic liquids," *Anal. Chem.*, vol. 82, no. 5, pp. 1680–1691, 2010, doi: 10.1021/ac9020159.

[43] A. J. Bard, L. R. a. Faulkner, and H. S. a. White, *Electrochemical Methods: Fundamentals and Applications / Allen J. Bard, Larry R. Faulkner, Henry S. White,* 3rd ed., 2022.

[44] I. Heller, J. Kong, H. A. Heering, K. A. Williams, S. G. Lemay, and C. Dekker, "Individual single-walled carbon nanotubes as nanoelectrodes for electrochemistry," *Nano letters*, vol. 5, no. 1, pp. 137–142, 2005, doi: 10.1021/nl048200m.

[45] R. C. Kubendran, S. Kim, and R. F. Yazicioglu, "Error correction algorithm for high accuracy bio-impedance measurement in wearable healthcare applications," in *2013 IEEE International Symposium on Circuits and Systems (ISCAS2013)*, Beijing, 2013, pp. 1292–1295.

[46] J. E. B. Randles, "Kinetics of rapid electrode reactions," *Discuss. Faraday Soc.*, vol. 1, p. 11, 1947, doi: 10.1039/DF9470100011.

[47] Z. Wang, A. Murphy, A. O'Riordan, and I. O'Connell, "Equivalent Impedance Models for Electrochemical Nanosensor-Based Integrated System Design," *Sensors (Basel, Switzerland)*, vol. 21, no. 9, 2021, doi: 10.3390/s21093259.

[48] A. Lasia, "The Origin of the Constant Phase Element," *The journal of physical chemistry letters*, vol. 13, no. 2, pp. 580–589, 2022, doi: 10.1021/acs.jpclett.1c03782.

[49] M. R. Shoar Abouzari, F. Berkemeier, G. Schmitz, and D. Wilmer, "On the physical interpretation of constant phase elements," *Solid State Ionics*, vol. 180, 14-16, pp. 922–927, 2009, doi: 10.1016/j.ssi.2009.04.002.

[50] T. Heil and A. Jossen, "Continuous approximation of the ZARC element with passive components," *Meas. Sci. Technol.*, vol. 32, no. 10, p. 104011, 2021, doi: 10.1088/1361-6501/ac0466.

[51] E. Kuhn, C. Forgez, P. Lagonotte, and G. Friedrich, "Modelling Ni-mH battery using Cauer and Foster structures," *Journal of Power Sources*, vol. 158, no. 2, pp. 1490–1497, 2006, doi: 10.1016/j.jpowsour.2005.10.018.

[52] H. Ren, Y. Zhao, S. Chen, and L. Yang, "A comparative study of lumped equivalent circuit models of a lithium battery for state of charge prediction," *Int J Energy Res*, 2019, doi: 10.1002/er.4759.

[53] Y. Hou, T. Guo, M. Bance, and C. Jiang, "A High-Precision Circuit-Simulator-Compatible Model for Constant Phase Element Using Rational Function Approximation," *IEEE J. Electron Devices Soc.*, vol. 11, pp. 726–733, 2023, doi: 10.1109/JEDS.2023.3292824.

[54] M. Berljafa and S. Güttel, "The RKFIT Algorithm for Nonlinear Rational Approximation," *SIAM J. Sci. Comput.*, vol. 39, no. 5, A2049-A2071, 2017, doi: 10.1137/15m1025426.

[55] W. Hendrickx and T. Dhaene, "A Discussion of "Rational Approximation of Frequency Domain Responses by Vector Fitting"," *IEEE Trans. Power Syst.*, vol. 21, no. 1, pp. 441–443, 2006, doi: 10.1109/TPWRS.2005.860905.

[56] D. Xue, C. Zhao, and Y. Chen, "A Modified Approximation Method of Fractional Order System," in *2006 International Conference on Mechatronics and Automation*, Luoyang, Henan, 2006, pp. 1043–1048.

[57] *NOVA.* [Online]. Available: https://www.metrohm.com/en_gb/service/software-center/nova.html (accessed: Jan. 29 2025).

[58] Y. Chao, H. Yue, B. L. Hassler, R. M. Worden, and A. J. Mason, "Amperometric electrochemical microsystem for a miniaturized protein biosensor array," *IEEE Trans. Biomed. Circuits Syst.*, vol. 3, no. 3, pp. 160–168, 2009, doi: 10.1109/TBCAS.2009.2015650.

[59] P. M. Levine, P. Gong, R. Levicky, and K. L. Shepard, "Active CMOS Sensor Array for Electrochemical Biomolecular Detection," *IEEE J. Solid-State Circuits*, vol. 43, no. 8, pp. 1859–1871, 2008, doi: 10.1109/JSSC.2008.925407.

[60] A. Manickam, A. Chevalier, M. McDermott, A. D. Ellington, and A. Hassibi, "A CMOS Electrochemical Impedance Spectroscopy (EIS) Biosensor Array," *IEEE transactions on biomedical circuits and systems*, vol. 4, no. 6, pp. 379–390, 2010, doi: 10.1109/TBCAS.2010.2081669.

[61] M. Schienle *et al.,* "A fully electronic DNA sensor with 128 positions and in-pixel A/D conversion," *IEEE J. Solid-State Circuits*, vol. 39, no. 12, pp. 2438–2445, 2004, doi: 10.1109/JSSC.2004.837084.

[62] A. Manickam *et al.,* "A CMOS Electrochemical Biochip With 32$\times$ 32 Three-Electrode Voltammetry Pixels," *IEEE J. Solid-State Circuits*, vol. 54, no. 11, pp. 2980–2990, 2019, doi: 10.1109/JSSC.2019.2941020.

[63] D. Djekic, G. Fantner, K. Lips, M. Ortmanns, and J. Anders, "A 0.1% THD, 1-M $\Omega$ to 1-G $\Omega$ Tunable, Temperature-Compensated Transimpedance Amplifier Using a Multi-Element Pseudo-Resistor," *IEEE J. Solid-State Circuits*, vol. 53, no. 7, pp. 1913–1923, 2018, doi: 10.1109/JSSC.2018.2820701.

[64] M. Haberle, D. Djekic, G. E. Fantner, K. Lips, M. Ortmanns, and J. Anders, "An Integrator-Differentiator TIA Using a Multi-Element Pseudo-Resistor in its DC Servo Loop for Enhanced Noise Performance," in *ESSCIRC 2018 - IEEE 44th European Solid State Circuits Conference (ESSCIRC)*, Dresden, 2018, pp. 294–297.

[65] Z. Wang, A. Wall, A. O'Riordan, D. O'Hare, G. M. Salgado, and I. O'Connell, "Models and Interfaces for Electrochemical Sensors: Architectures and Implementations," in *Biomedical Electronics, Noise Shaping ADCs, and Frequency References*, P. Harpe, A. Baschirotto, and K. A. Makinwa, Eds., Cham: Springer International Publishing, 2023, pp. 79–103.

[66] M. M. Ahmadi and G. A. Jullien, "Current-Mirror-Based Potentiostats for Three-Electrode Amperometric Electrochemical Sensors," *IEEE Trans. Circuits Syst. I*, vol. 56, no. 7, pp. 1339–1348, 2009, doi: 10.1109/TCSI.2008.2005927.

[67] S. Sutula, J. Pallares Cuxart, J. Gonzalo-Ruiz, F. X. Munoz-Pascual, L. Teres, and F. Serra-Graells, "A 25-µW All-MOS Potentiostatic Delta-Sigma ADC for Smart Electrochemical Sensors," *IEEE Trans. Circuits Syst. I*, vol. 61, no. 3, pp. 671–679, 2014, doi: 10.1109/TCSI.2013.2284179.

[68] M. Rajabzadeh, M. Haberle, A. Jain, and M. Ortmanns, "An Integrated Readout for Current Sensing based on a ΣΔ Modulator with Switched Capacitor Feedback," in *ESSCIRC 2019 - IEEE 45th European Solid State Circuits Conference (ESSCIRC)*, Cracow, Poland, 2019, pp. 321–324.

[69] M. A. Akram, A. Aberra, S.-J. Kweon, and S. Ha, "An Ultra-low-power Amplifier-less Potentiostat Design Based on Digital Regulation Loop," *IEEE Trans. Biomed. Circuits Syst.*, pp. 1–12, 2025, doi: 10.1109/TBCAS.2025.3527652.

[70] M. A. Akram, A. Aberra, S.-J. Kweon, and S. Ha, "3.6 An Amplifier-Less CMOS Potentiostat IC Consuming 3.7nW Power all over 129.5dB Dynamic Range for Electrochemical Biosensing," in *2024 IEEE International Solid-State Circuits Conference (ISSCC)*, San Francisco, CA, USA, 2024, pp. 64–66.

Authorized licensed use limited to: UNIVERSITY COLLEGE CORK. Downloaded on July 07,2025 at 14:33:53 UTC from IEEE Xplore. Restrictions apply.
© 2025 IEEE. All rights reserved, including rights for text and data mining and training of artificial intelligence and similar technologies. Personal use is permitted, but republication/redistribution requires IEEE permission. See https://www.ieee.org/publications/rights/index.html for more information.

This article has been accepted for publication in IEEE Transactions on Biomedical Circuits and Systems. This is the author's version which has not been fully edited and content may change prior to final publication. Citation information: DOI 10.1109/TBCAS.2025.3579698





**Zhongzheng Wang** (Student Member, IEEE) received the B.E. Degree in Electronics Science and Technologies from Beijing University of Chemical Technology (BUCT), Beijing, China in 2017, and completed his M.E. Degree in Electronics Engineering from IoE Research Group at University College Dublin (UCD), Dublin, Ireland in 2019. Currently, he is conducting Ph.D. research at Microelectronics Circuit Center of Ireland (MCCI), Cork, Ireland, and since 2024, he has worked as a Senior Analog Designer at Analog Devices, Limerick, Ireland.

His research focuses on new generation electrochemical sensor interface ICs, with an emphasis on fast EIS techniques, low-power electrochemical potentiostats and current readout ICs.

Mr. Wang was a recipient of Tyndall National Institute Wrixon Research Excellence Bursary 2023, IEEE SSCS Student Travel Grand Award for ISSCC 2022 & BioCAS 2024 and ADI Outstanding Student IC Designer Award 2022.



**Han Shao** (Member, IEEE) received her PhD from University College Cork in 2018 and currently working as a researcher at the Tyndall National Institute in Cork, Ireland.

Her work primarily focuses on the development of nanomaterial-based electrochemical sensors, with a particular emphasis on diverse agricultural applications. .

Dr. Shao was a recipient of the Research Emerging from a 3rd Level Institution Award at the National Ploughing Championships 2022 and the UCC Innovator of the Year award in the same year. Dr. Han was the WiSe co-chair at the IEEE APSCON 2024 conference, and currently is the temporary treasurer of IEEE UK&I Section 2024. She is also the leader of Bio-/chemical Sensors Cluster under IEEE Sensors Council.



**Alan O'Riordan** (Member, IEEE) received his PhD in Chemistry (Nanotechnology) from Univerisity College Cork, Cork, Ireland in 2005. He is currently a head and a Senior Research Fellow of the Precision Electrochemical Nanosensor Group at the Tyndall National Institute and also a Principal Investigator for Smart Agri-food and Nanosensors & Systems.

His research fields cover two complementary sensor technologies on silicon chip substrates that employ (i) nano-electrochemistry and (ii) Surface enhanced Raman Spectroscopy detection mechanisms that providing highly sensitive, selective and reliable measurements. The research topics focus on developing smart sensors and systems for Sustainable Agri-food and Environmental applications.

Prof. O'Riordan has competitively won multiple research projects worth circa ~€25M in total research funding to the PI, and has published over 100 peer reviewed publications, one patent granted "Nanowire Electrode Sensor" EU & US (US 20140145709) and won the Enterprise Ireland Gold Medal for Most Innovative Technology Emerging from Third Level (National Ploughing Contest 2016/2022).



**Javier Higes-Marquez** (Member, IEEE) received a M.Sc. degree in Telecommunication Engineering from the University of Sevilla in 2014 and an inter-university M.Sc. in Security of Information and Communication Technologies from the Open University of Catalonia and the Autonomous University of Barcelona in 2018.

His experience is related to data converter setup and characterization and embedded and radio communication systems. His research interests are related to the development of portable electronics systems that integrate with electrochemical nanosensors.



**Ivan O'Connell** (Senior Member, IEEE) received the B.E. and Ph.D. degrees from the University College Cork in 1998 and 2005, respectively. He is currently working with Altera, Ireland, as part of their Technology Pathfinding Group. His primary research interests are in the area of analogue mixed-signal circuits and data converters and high-speed communication links.

From 2022 to 2024 he was Director of Mixed Signal Design in Analog Devices Ireland. Prior to which he was Head of Precision Circuits and Cryo-CMOS in MCCI, Tyndall National Institute, Cork, Ireland, which consisted of Masters' and Ph.D. students, Post-doctoral Researchers, Research Assistants and Senior Researchers. Where, in addition to being the Head of Group of the MCCI core research team he was also Principal Investigator for numerous Enterprise Ireland funded Innovation Partnerships and Commercialisation Funds. He was also a Funded Investigator in the Science Foundation Ireland (SFI) funded CONNECT and VistaMilk centres. Prior to joining MCCI, Tyndall National Institute in 2013, he was the Design Manager with ChipSensors Ltd., Ireland, which was acquired by Silicon Laboratories in 2010. In ChipSenors he played a lead role in the development of their digital relative humidity and temperature sensor products and their subsequent commercialisation.

Dr. O'Connell is currently an Associate Editor with the IEEE Transactions on Circuits and Systems I. In 2018, his work was recognised by Science Foundation Ireland with their Industry Partnership Award, which celebrates collaboration between SFI funded academic research groups and industry.

Authorized licensed use limited to: UNIVERSITY COLLEGE CORK. Downloaded on July 07,2025 at 14:33:53 UTC from IEEE Xplore. Restrictions apply.
© 2025 IEEE. All rights reserved, including rights for text and data mining and training of artificial intelligence and similar technologies. Personal use is permitted, but republication/redistribution requires IEEE permission. See https://www.ieee.org/publications/rights/index.html for more information.

This article has been accepted for publication in IEEE Transactions on Biomedical Circuits and Systems. This is the author's version which has not been fully edited and content may change prior to final publication. Citation information: DOI 10.1109/TBCAS.2025.3579698





**Daniel O'Hare** (Senior Member, IEEE) received the BE degree in Electronic Engineering from University College Dublin, Ireland, in 2000 and completed his PhD at the University of Limerick in 2017.

He joined Motorola Semiconductor 2000 and from 2004 to 2008 he was with Freescale Semiconductor designing ADCs and DACs for Cellular transceivers. From 2008 to 2012 he was with M4S NV a spinout of IMEC and from 2013 to 2017 he was an ADC researcher in the Circuits and Systems group at the University of Limerick. He is currently a Principal Researcher in the Microelectronic Circuits Centre Ireland (MCCI) based at the Tyndall National Institute, University College Cork. His research is in low-noise sensor interface circuits and integrated circuits to enable medical systems. This includes the design of low voltage, low noise, data-converters and analogue signal conditioning circuits.

Dr. O'Hare was co-recipient of the 2021 NEWCAS best student paper. Daniel was the recipient of the 2023 Tyndall mentor of the year award. He has more than 15 published papers and 2 granted Patents.

Authorized licensed use limited to: UNIVERSITY COLLEGE CORK. Downloaded on July 07,2025 at 14:33:53 UTC from IEEE Xplore. Restrictions apply.
© 2025 IEEE. All rights reserved, including rights for text and data mining and training of artificial intelligence and similar technologies. Personal use is permitted, but republication/redistribution requires IEEE permission. See https://www.ieee.org/publications/rights/index.html for more information.